Development of a High-Throughput Protein Interaction Assay and its Applications

Thesis by

Hanqing Li

In Partial Fulfillment of the Requirements for

the degree of

Doctor of Philosophy

CALIFORNIA INSTITUTE OF TECHNOLOGY

Pasadena, California

2017

(Defended 18th April 2017)

ACKNOWLEDGEMENTS

First and foremost, I would like to thank my advisor, Dr. Kai Zinn, for all the advice and support he has given me over the years. I could not have asked for a better advisor in my graduate school career. I would also like to give my heartfelt thanks to the members of my committee, Dr. Scott Fraser, Dr. Paul Sternberg, and Dr. Ray Deshaies, for their encouragement and guidance, both personal and professional. I am also forever grateful to all the friends and colleagues I have met at Caltech. You have all helped make my years here enjoyable and enlightening. Last, but not least, my love and gratitude to my family, who have been there for me through thick and thin.

Abstract

Protein-protein interactions (PPIs) form the backbone for a vast array of biological processes in an organism, ranging from signal transduction to gene regulation to intercellular signaling. Therefore, mapping out protein interactomes has been a crucial and prolific area of scientific research. In recent years, much progress has been made in generating high throughput protein interaction data in a variety of organisms, including *S. cerevisiae*, *C. elegans*, and *D. melanogaster*, as well as in human cell culture. The strength of protein interactions varies widely, from almost irreversible assembly of complexes to highly transient interactions. Because of their diversity and complexity, a wide variety of methods have been used to study protein interactions. This includes such commonly-used assays like yeast two-hybrid, to mass spectrometry, ELISA, affinity pulldowns, etc.

Despite the plethora of assays and data sets generated for PPIs, interactions involving cell surface and secreted proteins (CSSPs) remains underrepresented in the results. This is due to the fact that CSSP interactions tend to have lower K_{DS} (around the μM range), and are generally highly transient and difficult to perform using standard assays such as yeast two-hybrid. To circumvent these problems, we designed a high-throughput PPI assay with high sensitivity. To validate the effectiveness of the assay, we utilized it to probe for interactions among two families of *Drosophila* CSS proteins, the Beats and the Sides, to see if we could recapitulate known interactions and uncover new ones. We were able to recapitulate almost all of the known interactions, as well as discover three novel ones. Additionally, we also studied the expression patterns of members of the Beat and

Side families in *Drosophila* embryos and larvae, as well as analyzed the effects of mutations of Side-VI and Beat-Vs in embryos.

TABLE OF CONTENTS

Chapter 1

Introduction

Proteins are the worker molecules, and the workhorses, of cells. Protein-protein interactions (PPIs) are responsible for a multitude of different processes in an organism, from signal transduction [1, 2] to regulation of gene expression [3] to cell growth and differentiation [2, 4, 5]. PPIs vary widely in their biophysical characteristics. They can form homo-oligomeric and hetero-oligomeric interactions (depending on how many different subunits the protein is comprised of), and can range from highly stable complexes to transient interactions [6]. Aberrations in PPIs can lead to a variety of diseases in humans, including Huntington's disease [7], Alzheimer's [8], and cancer [9]. As proteins involved in disease are often the target of various therapies [10], a comprehensive knowledge of the human protein interactome is indispensable. In recent years, advances in various protein interaction assays have enabled us to re-construct the interactomes in a variety of organisms, including *D. melanogaster* [11, 12], *C. elegans* [13, 14], *S. cerevisiae* [15-18], and humans [19-21].

Overview of Protein Interaction Assays

A variety of genetic and biochemical methods exist to identify PPIs. Some common ones are summarized below.

Yeast Two-Hybrid (Y2H)

One of the most widely used assays to detect PPIs is the yeast two-hybrid system [22]. This assay utilizes the binding of a transcription factor to an upstream activating sequence

(UAS) to drive expression of a downstream reporter gene. The DNA-binding domain (BD) of the transcription factor is fused to the bait protein and the activating domain (AD) is fused to the prey protein. If the bait and prey proteins interact, the BD and AD are brought into close proximity and expression of the reporter gene is initiated. The Y2H assay is advantageous in that it is relatively simple to perform and is amenable to screening of many protein pairs. Disadvantages include a high false positive rate and inapplicability to membrane proteins, etc. Various versions of this assay exist, including the split-ubiquitin yeast two-hybrid [23] and the fluorescent two-hybrid technique [24].

Enzyme-Linked Immunosorbent Assay (ELISA)

The enzyme-linked immunosorbent assay (ELISA) utilizes an enzyme as the reporter label and is ubiquitously performed in labs and diagnostics around the world [25]. Several variations of this assay exist but the basic principle is similar. Briefly, individual wells are coated with a capture antibody and bait proteins with the requisite tags are captured by the antibody and immobilized on the surface of the well. The well is then incubated with the prey protein fused to a different tag. Finally, an enzyme-fused antibody which recognizes the tag on the prey protein is incubated in the well. A substrate of the enzyme is then added and the resulting color change determines if the bait and prey have interacted.

Affinity Purification-Mass Spectrometry (AP-MS)

This technique is useful for the identification of multi-protein complexes [26]. Protein complexes can be pulled down using protein-specific antibodies or antibodies recognizing a tag on the protein of interest. The purified complex is then analyzed with mass spectrometry. One recent advance to this method is the tandem affinity purification method (TAP) [27]. In this method, two tags are used: a protein A (ProtA) tag and calmodulin-binding peptide (CBP) upstream of the ProtA. These two tags are separated by a TEV recognition sequence. In the first purification round, proteins are pulled down with protein A. The protein complex is then

cleaved with TEV protease and a second round of purification is performed using calmodulin coated beads. These two rounds of purification ensure that the level of contaminating proteins is minimized. The final purified protein complex is then analyzed with mass spectrometry.

Fluorescence Resonance Energy Transfer (FRET)

Fluorescence resonance energy transfer (FRET) is a technique that is useful for analyzing PPIs, even in real time [28]. One target protein is fused to a fluorescent donor protein and the other is fused to a fluorescent acceptor protein. If the two proteins of interest interact, non-radiative energy transfer occurs between the donor and acceptor proteins, which can then be measured.

Other Assays

A variety of other assays are also available to study PPIs, such as surface plasmon resonance (SPR), microarrays, and ultracentrifugation.

Cell Surface and Secreted Proteins

With the completion of the sequencing of the human genome, deciphering the identity and function of the proteins encoded by the uncovered genes are of paramount importance. Cell surface and secreted proteins (CSSPs) played a major role in the evolution of multicellular organisms, facilitating communication and task sharing between individual cells in an organism [29]. It is estimated that around 7000 genes in humans encode CSS proteins [30]. CSSPs play a plethora of roles in different cellular processes, such as cellular signaling, differentiation, morphogenesis, as well as maintaining structural integrity between cells. Common families of CSSPs include growth factors [31, 32], cytokines [33], as well as various receptors and transporters. These proteins are also utilized by various pathogens to initiate the

infection process and are also important in diseases, such as cancer progression. Due to these characteristics, and their accessibility in the extracellular space, CSSPs are often important targets for drugs and therapeutics. Indeed, a number of treatments targeting CSSPs are already available, such as Rituxan for non-Hodgkin's lymphoma and Herceptin for breast cancer [34].

Despite their importance, CSSPs have long been underrepresented in high-throughput protein screens [35]. This is mainly due to certain peculiar biochemical properties of CSSPs and the interactions they are involved in. CSSPs often contain disulfide bonds, made possible by the oxidizing environment of the extracellular space; additionally many of these proteins are also glycosylated [36]. These properties make it difficult to detect CSSP interactions with cell-based assays such as Y2H. CSSPs also often contain hydrophobic transmembrane domains as well as hydrophilic domains, which makes them difficult to solubilize for assays such as mass spectrometry. Interactions comprised of CSSPs are also often relatively weak (K_D ~μM) [37], which makes them hard to detect using many traditional assays. A possible explanation for the low affinity of CSSP interactions is that because many of these proteins are embedded in the cell membrane, high local concentration of the protein strengthens interactions through avidity [36].

Despite these challenges, multiple methods have been developed to facilitate the identification of CSSP interactions, including SPR and ultracentrifugation. However, many of these assays are not amenable to large scale screens, as they require a large amount of purified protein. Another popular technique is the utilization of avidity to increase binding affinity. Multimerization domains utilized include ones that form dimers (such as Fc domain), trimers, and pentamers, such as the rat cartilage oligomeric matrix protein (COMP) [38-40]. Multimerization has been especially successful when coupled with ELISA assays. A recent screen of *Drosophila* CSSPs was performed using Fc fusions as bait and COMP pentamer

fusions as prey; 83 novel interactions were discovered using this method [41]. Another ELISA screen, named AVEXIS, was successfully performed on zebrafish IgSF proteins [38].

Overview of the Bio-Plex System

The Bio-Plex system from Bio-Rad utilizes Luminex xMap technology and combines optics, fluidics, and digital signal processing to enable the development of multiplexed assays. The Bio-Plex 200 system used in this assay consists of 100 types of spectrally-distinct beads, called bead regions. Each polystyrene bead region is 6.5 μm and is composed of a magnetic core, as well as being coated with a different ratio of two fluorescent dyes, which emits a distinct fluorescent signal when excited by a laser. The beads are carboxylated, which enables them to be coupled to proteins via free lysine residues using standard EDC-NHS chemistry, or to modified nucleic acids. Coupled beads can be used to perform a number of different multiplexed assays.

The final step of every assay entails the addition of a detection antibody coupled to phycoerythrin, a fluorescent protein. The multiplexed beads are transferred to 96-well plates, and fed into the Bioplex machine. The beads flow single file through the machine, which is composed of two lasers: one which classifies the beads and the other which detects the phycoerythrin signal. Another version of the Bio-Plex system, the Bio-Plex 3D, contains 500 different spectrally-distinct bead regions, enabling the analysis of up to 500 analytes simultaneously.

References

1. Bu, Z. and D.J.E. Callaway, *Chapter 5 - Proteins MOVE! Protein dynamics and long-range allostery in cell signaling*, in *Advances in Protein Chemistry and Structural Biology*, D. Rossen, Editor. 2011, Academic Press. p. 163-221.

2. Johnson, G.L. and R.R. Vaillancourt, *Sequential protein kinase reactions controlling cell growth and differentiation.* Current Opinion in Cell Biology, 1994. **6**(2): p. 230-238.

3. Maniatis, T., S. Goodbourn, and J. Fischer, *Regulation of inducible and tissue-specific gene expression.* Science, 1987. **236**(4806): p. 1237-1245.

4. Henriksson, M. and B. Lüscher, *Proteins of the Myc Network: Essential Regulators of Cell Growth and Differentiation*, in *Advances in Cancer Research*, F.V.W. George and K. George, Editors. 1996, Academic Press. p. 109-182.

5. Moustakas, A., et al., *Mechanisms of TGF-β signaling in regulation of cell growth and differentiation.* Immunology Letters, 2002. **82**(1–2): p. 85-91.

6. Nooren, I.M.A. and J.M. Thornton, *Diversity of protein–protein interactions.* The EMBO Journal, 2003. **22**(14): p. 3486-3492.

7. Giorgini, F. and P.J. Muchowski, *Connecting the dots in Huntington's disease with protein interaction networks.* Genome Biology, 2005. **6**(3): p. 210-210.

8. Querfurth , H.W. and F.M. LaFerla *Alzheimer's Disease.* New England Journal of Medicine, 2010. **362**(4): p. 329-344.

9. Croce , C.M., *Oncogenes and Cancer.* New England Journal of Medicine, 2008. **358**(5): p. 502-511.

10. Lagerstrom, M.C. and H.B. Schioth, *Structural diversity of G protein-coupled receptors and significance for drug discovery.* Nat Rev Drug Discov, 2008. **7**.

11. Giot, L., et al., *A Protein Interaction Map of Drosophila melanogaster.* Science, 2003. **302**(5651): p. 1727-1736.

12. Guruharsha, K.G., et al., *A Protein Complex Network of Drosophila melanogaster.* Cell, 2011. **147**(3): p. 690-703.

13. Li, S., et al., *A Map of the Interactome Network of the Metazoan C. elegans*. Science, 2004. **303**(5657): p. 540-543.

14. Simonis, N., et al., *Empirically controlled mapping of the Caenorhabditis elegans protein-protein interactome network*. Nat Meth, 2009. **6**(1): p. 47-54.

15. Ho, Y., et al., *Systematic identification of protein complexes in Saccharomyces cerevisiae by mass spectrometry.* Nature, 2002. **415**(6868): p. 180-183.

16. Krogan, N.J., et al., *Global landscape of protein complexes in the yeast Saccharomyces cerevisiae.* Nature, 2006. **440**(7084): p. 637-643.

17. Tarassov, K., et al., *An in Vivo Map of the Yeast Protein Interactome.* Science, 2008. **320**(5882): p. 1465-1470.

18. Uetz, P., et al., *A comprehensive analysis of protein-protein interactions in Saccharomyces cerevisiae.* Nature, 2000. **403**(6770): p. 623-627.

19. Rual, J.-F., et al., *Towards a proteome-scale map of the human protein-protein interaction network*. Nature, 2005. **437**(7062): p. 1173-1178.

20. Stelzl, U., et al., *A human protein-protein interaction network: a resource for annotating the proteome.* Cell, 2005. **122**.

21. Ewing, R.M., et al., *Large-scale mapping of human protein–protein interactions by mass spectrometry*. Molecular Systems Biology, 2007. **3**(1).

22. Fields, S. and O.-k. Song, *A novel genetic system to detect protein-protein interactions.* Nature, 1989. **340**(6230): p. 245-246.

23. Stagljar, I., et al., *A genetic system based on split-ubiquitin for the analysis of interactions between membrane proteins in vivo.* Proceedings of the National Academy of Sciences, 1998. **95**(9): p. 5187-5192.h

24. Zolghadr, K., et al., *A Fluorescent Two-hybrid Assay for Direct Visualization of Protein Interactions in Living Cells.* Molecular & Cellular Proteomics, 2008. **7**(11): p. 2279-2287.

25. Lequin, R.M., *Enzyme Immunoassay (EIA)/Enzyme-Linked Immunosorbent Assay (ELISA).* Clinical Chemistry, 2005. **51**(12): p. 2415-2418.

26. Bauer, A. and B. Kuster, *Affinity purification-mass spectrometry.* European Journal of Biochemistry, 2003. **270**(4): p. 570-578.

27. Rigaut, G., et al., *A generic protein purification method for protein complex characterization and proteome exploration.* Nat Biotech, 1999. **17**(10): p. 1030-1032.

28. Petschnigg, J., J. Snider, and I. Stagljar, *Interactive proteomics research technologies: recent applications and advances.* Current Opinion in Biotechnology, 2011. **22**(1): p. 50-58.

29. Ben-Shlomo, I., et al., *Signaling receptome: a genomic and evolutionary perspective of plasma membrane receptors involved in signal transduction.* Sci STKE, 2003. **2003**.

30. Diehn, M., et al., *Genome-Scale Identification of Membrane-Associated Human mRNAs.* PLoS Genetics, 2006. **2**(1): p. e11.

31. Cross, M.J. and L. Claesson-Welsh, *FGF and VEGF function in angiogenesis: signalling pathways, biological responses and therapeutic inhibition.* Trends in Pharmacological Sciences, 2001. **22**(4): p. 201-207.

32. Ornitz, D.M. and N. Itoh, *Fibroblast growth factors.* Genome Biology, 2001. **2**(3): p. reviews3005.1.

33. Schooltink, H. and S. Rose-John, *Cytokines as therapeutic drugs.* J Interferon Cytokine Res, 2002. **22**(5): p. 505-16.

34. Clark, H.F., et al., *The Secreted Protein Discovery Initiative (SPDI), a Large-Scale Effort to Identify Novel Human Secreted and Transmembrane Proteins: A Bioinformatics Assessment*. Genome Research, 2003. **13**(10): p. 2265-2270.

35. Braun, P., et al., *An experimentally derived confidence score for binary protein-protein interactions.* Nat Meth, 2009. **6**(1): p. 91-97.

36. Wright, G.J., *Signal initiation in biological systems: the properties and detection of transient extracellular protein interactions †This article is part of a Molecular BioSystems themed issue on Computational and Systems Biology.* Molecular Biosystems, 2009. **5**(12): p. 1405-1412.

37. Anton van der Merwe, P. and A. Neil Barclay, *Transient intercellular adhesion: the importance of weak protein-protein interactions.* Trends in Biochemical Sciences, 1994. **19**(9): p. 354-358.

38. Bushell, K.M., et al., *Large-scale screening for novel low-affinity extracellular protein interactions.* Genome Res, 2008. **18**.

39. Holler, N., et al., *Development of improved soluble inhibitors of FasL and CD40L based on oligomerized receptors.* Journal of Immunological Methods, 2000. **237**(1–2): p. 159-173.

40. Voulgaraki, D., et al., *Multivalent recombinant proteins for probing functions of leucocyte surface proteins such as the CD200 receptor.* Immunology, 2005. **115**(3): p. 337-346.

41. Özkan, E., et al., *An Extracellular Interactome of Immunoglobulin and LRR Proteins Reveals Receptor-Ligand Networks.* Cell, 2013. **154**(1): p. 228-239.

Chapter Two
Development of a High-Throughput Assay to Measure Protein-Protein Interactions

Introduction

Protein-protein interactions form the backbone for a vast array of processes in an organism, ranging from signal transduction to gene regulation to intercellular signaling. Therefore, mapping out protein interactomes has been a crucial and prolific area of research. Progress has been made in generating high throughput protein interaction data in a variety of organisms, including *S. cerevisiae* [1], *C. elegans* [2, 3], and *D. melanogaster* [4, 5]. The strength of protein- protein interactions varies widely, from extremely stable complexes, to highly transient interactions [6]. Because of their diversity and complexity, a variety of different methods have been developed to study PPIs. This includes the commonly-used yeast two-hybrid assay, mass spectrometry, and ELISA, among others.

With the completion of human genome project, it is estimated that around a fifth of human genes encode cell surface and secreted proteins [7]. These proteins play an indispensable role in various processes involving cells, including the flow of information between cells and their environments. Due to their importance and accessibility, CSSPs are often the target of drugs and other therapeutics, including the non-Hodgkin's lymphoma drug Rituxan and the breast cancer drug Herceptin [8]. However, certain biochemical traits of CSSPs and their interactions have made them elusive to many of the commonly used techniques employed in PPI detection and they are often underrepresented in large-scale studies of protein interactomes [4, 9, 10]. There are several reasons that interactions among CSSP interactions are hard to detect. First, these proteins are often glycosylated and consist of disulfide bonds, which make them difficult to recapitulate in the reducing environment of cell-

based assays such as Y2H [11]. CSSP interactions are also often highly transient and weak (K_D in the μM range) [12], which makes them difficult to study with techniques which require stringent wash steps. Lastly, the insoluble transmembrane domains on cell surface proteins preclude their purification with standard biochemical techniques, which makes them difficult to study with methods such as mass spectrometry [13].

Despite these difficulties, recent advances have been made to facilitate the study of CSSP interactions. One important method involves the oligomerization of extracellular domains of these proteins into dimers, trimers and pentamers, to increase the avidity of these interactions [14-16]. These methods have shown to be incredibly effective, often increasing the binding signals by many orders of magnitude. A large scale ELISA study of three families of *Drosophila* CSSPs by Ozkan et al. [17], dubbed the ECIA, utilizes dimers and pentamers as bait and prey, respectively, resulting in the detection of 83 previously unknown interactions. In this study, we build on these techniques by coupling the power of avidity with the Bio-Rad Bio-Plex® 200 system to develop a high-throughput protein-protein interaction assay that has increased sensitivity, minimizes protein and reagent usage, and expedites the experimental process. We utilized this assay to screen for interactions among the *Drosophila* Beat and Side families, two families of proteins that were included in the original ECIA data. Although many novel interactions were discovered in the ECIA, many members of these families remain orphans. Our goal was to see if we could de-orphanize some of these proteins using Bio-Plex assay. We were able to recapitulate most of the interactions found in the ECIA, and also discovered three novel interactions.

Results

The Bio-Plex system and development of the assay

The Bio-Rad Bio-Plex® 200 system utilizes the xMAP® platform developed by Luminex. It is based on the principles of flow cytometry, and combines optics, digital signal processing, and fluidics to enable the development of high-throughput, multiplexed assays. Central to the process are the 6.5 μm, polystyrene bead regions, each of which is coated with a different ratio of two fluorescent dyes, which renders them spectrally-distinct when excited by a laser. The Bio-Plex® 200 system used in this assay is composed of 100 different bead regions, allowing for the analysis of up to 100 distinct analytes simultaneously, while the Bio-Plex® 3D system is composed of 500 bead regions and allows for the analysis of up to 500 different analytes. The beads also contain a magnetic core, which facilitates their manipulation using magnetic separators, and are coated with surface carboxyl groups, enabling them to be conjugated to proteins via free lysine residues or to modified nucleic acids. Once conjugated to their protein targets, the beads can then be used in a multitude of different assays, all of which involve the final step of staining with a phycoerythrin-coupled antibody, before being fed into the Bio-Plex machine. The beads flow through the machine in single file, and are analyzed by two lasers: one to discern the identity of the bead region, and the other to detect phycoerythrin signal.

To increase the sensitivity of the assay, we utilized multimerization techniques similar to those described in Ozkan et al [17]. The constructs we used to generate bait proteins consist of the extracellular domain (ECD) of different baits fused to alkaline phosphatase (AP) and rat cartilage oligomeric matrix protein, COMP, a pentamerization domain that has been shown to dramatically increase the sensitivity of interaction assays [7, 18]. For prey, we used constructs where the ECD of different preys were fused to human Fc, enabling the formation of dimers. Since prey constructs also contain a C-terminal V5 tag, a V5 antibody was used to detect binding, followed by a secondary antibody conjugated to phycoerythrin.

There are two ways to attach the bait proteins to the beads: by direct coupling or by capturing with an antibody. Since our bait proteins are all relatively large, and should theoretically contain multiple free lysine residues, direct coupling was tried first. Bait proteins were expressed in *Drosphila* Schneider 2 (S2) cells and the secreted proteins purified from media using Ni resin. Each different bait protein was then conjugated to a specific bead region via standard EDC-NHS chemistry. Anti-AP antibody was added to the coupled beads, followed by phycoerythrin-coupled secondary and run on the Bio-Plex machine. We found that this direct coupling method was not optimal, as different bait proteins coupled to the beads with vastly different efficiencies (data not shown), and much protein was lost during the purification steps. To bypass direct coupling, we used the antibody-capture method (Fig 1). To accomplish this, we tagged the C-terminus of each of our bait constructs with an Avitag™, a 15 amino acid tag that is recognized by the enzyme biotin ligase (BirA), which then proceeds to add one biotin molecule to the tag [19-21]. This enzymatic biotinylation is preferable to the other commonly used chemical biotinylation, as it allows for the control of location and number of biotin molecules added per protein molecule. To perform in vivo biotinylation, we co-transfected the bait constructs with an ER-localized BirA construct optimized for expression in S2 cells [22]. To capture the bait proteins, we coupled different bead regions to streptavidin, and each bead region was incubated with a different biotinylated bait protein directly from the media, therefore bypassing the purification step. Each Fc-tagged prey protein was also expressed in S2 cells, and purified with Ni resin.

The bait-coated beads were then mixed and aliquoted and a different Fc prey protein added to each bead mixture. The reactions were then stained with anti-V5, followed by phycoerythrin-coupled secondary, and transferred to a 96-well plate and read with the Bio-Plex.

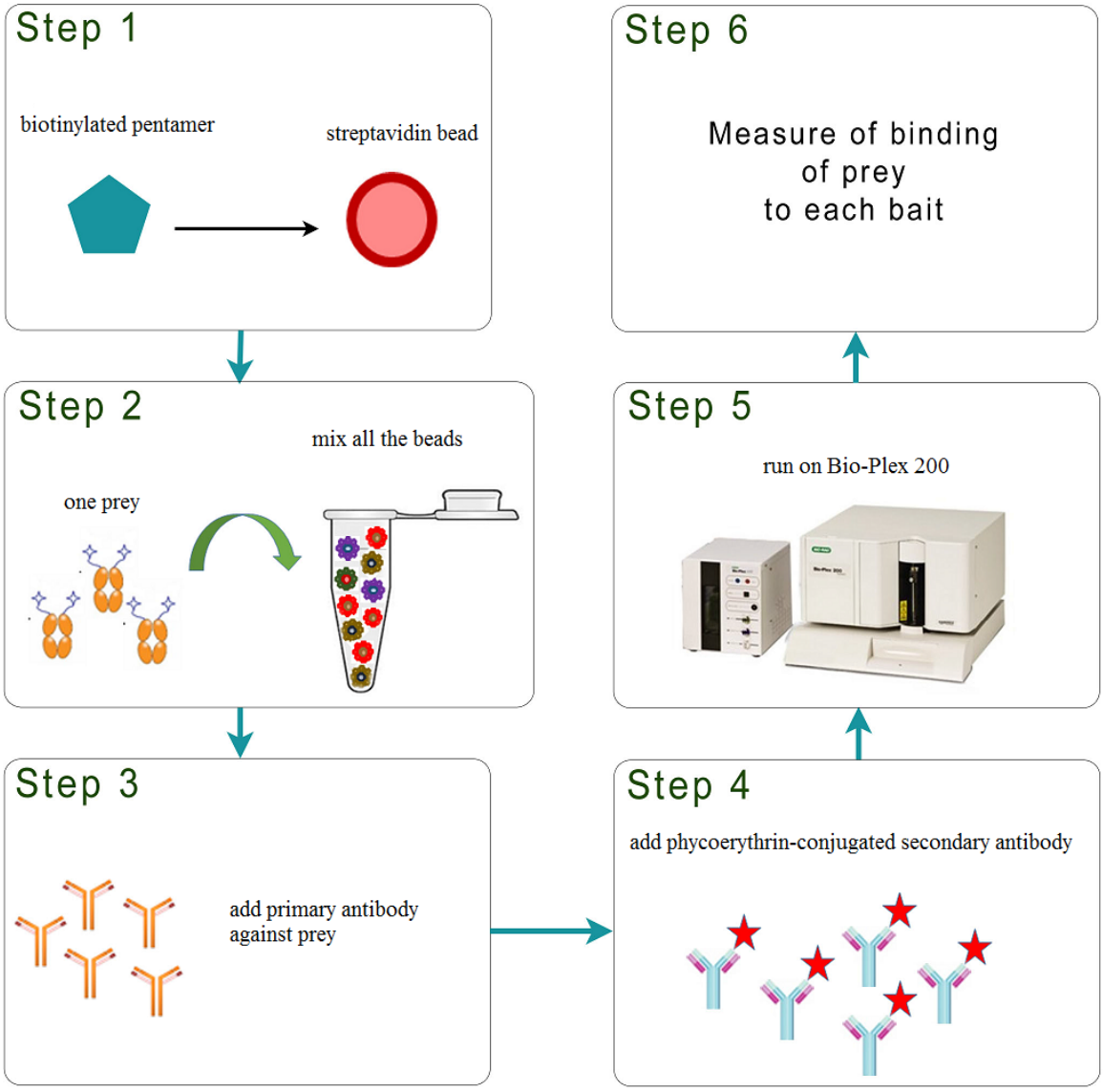

Figure 1: Schematic of Bio-Plex assay.

Biotinylated prey are captured with streptavidin-coupled beads and mixed. A single prey protein is added to the bead mixture and incubated overnight. The beads are then washed and stained with a primary antibody against

the prey, followed by a phycoerythrin-conjugated secondary antibody. The reaction is then analyzed on the Bio-Plex.

No protein "jumping" between bead regions

The biotin-streptavidin interaction is one of the strongest non-covalent interactions known in nature, with a K_D on the order of $\sim 10^{-14}$ mol/L [23], and is often used in many biochemical assays. Since the different bait-captured bead regions are being mixed before the addition of prey protein, we wanted to make sure that there would be no "jumping" of proteins from one bead region to another, as that would confound the results of the assay. To test whether or not there is jumping of proteins between bead regions, we coupled four different bead regions to streptavidin. To three of the streptavidin-coupled bead regions, we captured three pentamerized, biotinylated proteins, respectively. The beads were then mixed together and incubated overnight with anti-AP antibody, followed by phycoerythrin-coupled secondary, and run on the Bio-Plex. Strong phycoerythrin signal was detected for the bead regions with captured bait protein, while the streptavidin beads with no bait protein had almost no detectable signal (Fig. 2). These results show that there is no protein jumping between different bead regions.

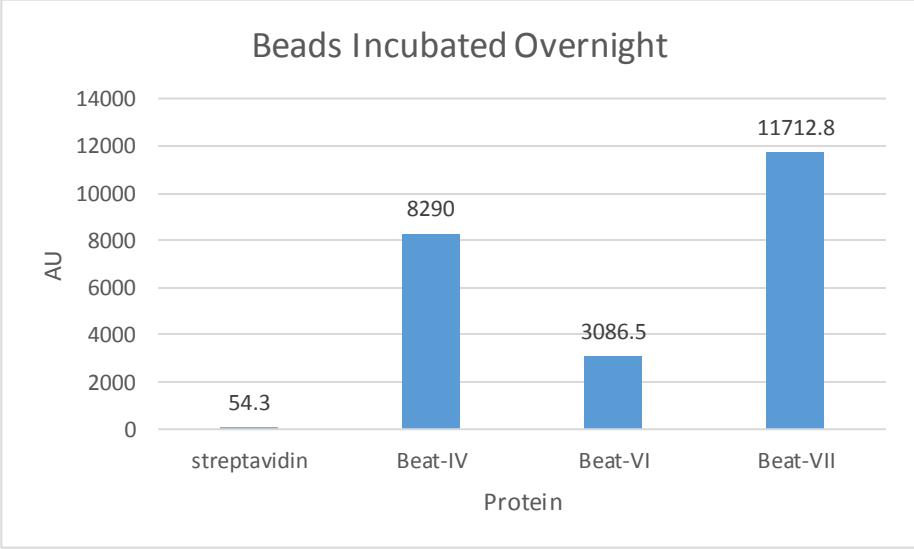

Figure 2: No protein "jumping" between bead regions

Biotinylated Beat-IV, Beat-VI, and Beat-VII bait proteins were captured with different streptavidin-coupled regions and mixed overnight with anti-AP antibody. The mixture was then incubated with phycoerythrin-coupled secondary antibody and run on the Bio-Plex. Bead regions with captured protein exhibited strong signal, while the streptavidin-coupled beads did not.

Screen for interactions between *Drosophila* Beats and Sides

The *Drosophila* Beaten Path protein family consists of 14 members, and is part of the Drosophila IgSF [24]. The first discovered member of this family is Beat-Ia, a cell adhesion molecule (CAM) which has been shown to facilitate motor axon defasciculation in *Drosophila* embryos [25]. The other members of the Beat family have been shown to exhibit differential expression in the CNS, motor neurons, and muscles in Drosophila embryos [24]. The Sidestep protein (Side) is also a member of the *Drosophila* IgSF and has been shown to be expressed in a variety of cells in the embryo, including muscles [26]. Side has also been shown to interact with Beat-Ia in vivo to regulate motor axon defasciculation [27]. Side is a member of a family of eight proteins [28, 29], and it is theorized that the members of the Side and Beat families might form an interaction network to aid in *Drosophila* nervous system development. The *Drosophila* interactome assay performed by Ozkan et al. verified this theory in part by uncovering more interactions among members of the Beat and Side families [17]. Despite this, many members of the families remained orphans.

We performed the Bio-Plex assay on the Beat and Side protein families first to see if we could recapitulate the interactions previously discovered, and second to see if our assay could uncover previously unknown interactions. 23 different pentameric bait constructs were co-transfected with BirA in S2 cells, and the protein-containing media harvested. The different bait proteins were then captured directly from media using different streptavidin-coupled bead regions and mixed. For prey, 23 different Fc-tagged constructs were transfected into S2 cells,

and purified with Ni resin. The pooled beads were aliquoted into Eppendorf tubes, and a different prey protein added to each tube; using this method, we were able to analyze each potential interaction pair in two orientations, with protein A as bait and protein B as prey, and vice versa. The reaction was then incubated overnight and stained with anti-V5 antibody, followed by a phycoerythrin-coupled secondary antibody, transferred to a 96-well plate and analyzed with the Bio-Plex.

Beats interact with Sides to form a protein interaction network

Using the Bio-Plex assay, we were able to recapitulate all interactions discovered in Ozkan et al, except for one (Fig. 3A). The interaction which we were not able to recapitulate involves the long-known one between Side and Beat-Ia. Although this interaction was strong in one orientation, it was undetectable in the reverse orientation, possibly due to the fact that Beat-Ia capture by streptavidin-coupled beads was not very effective. In addition to the known interactions, we also discovered three previously unknown ones: Beat-Ic--Side, Beat-Ic--Side-III, and Beat-VI--Side-II (Fig. 3B). These results show that our assay has at least comparable sensitivity as the ECIA.

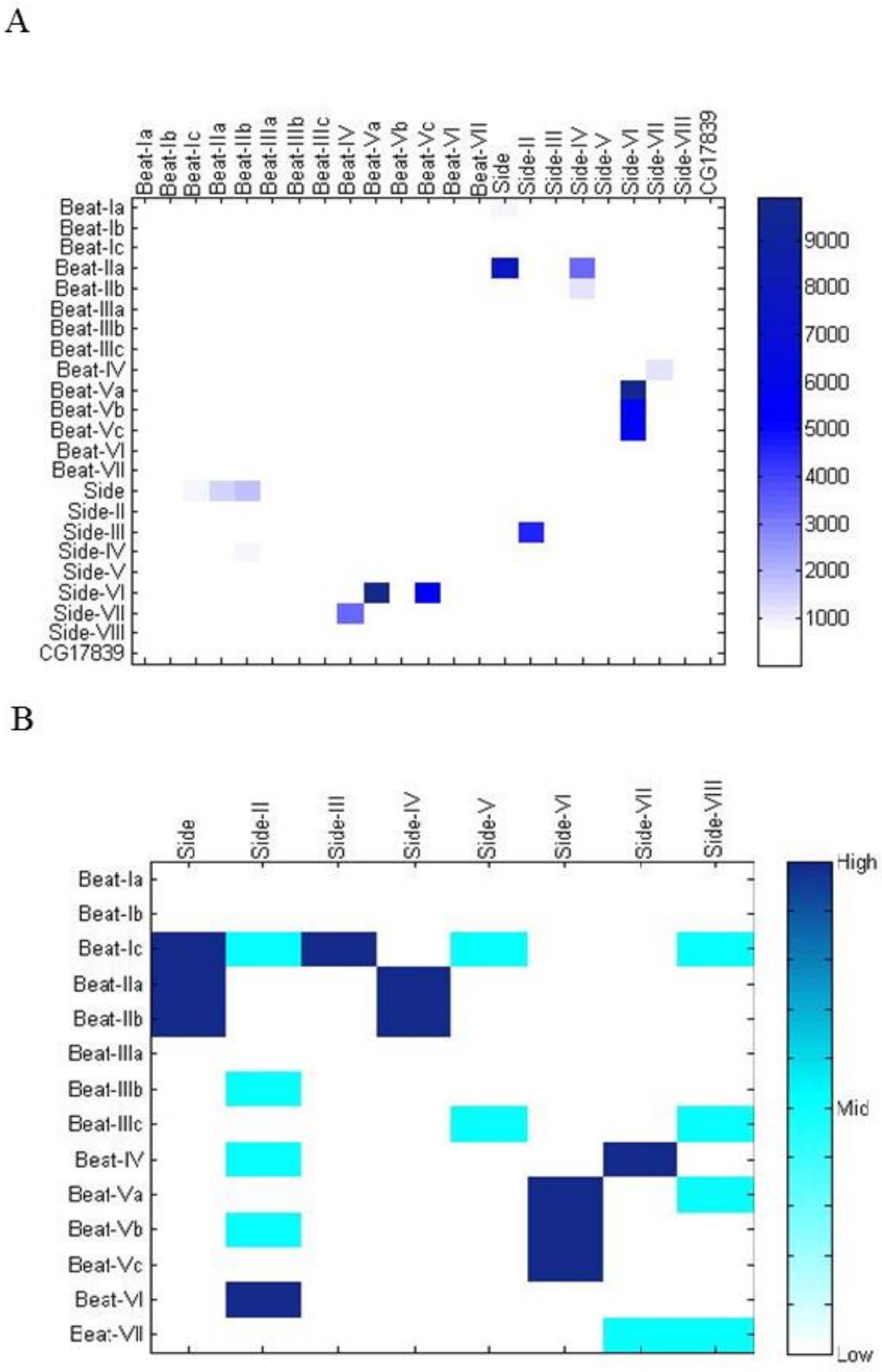

Figure 3: Heat maps of Beat and Side interactions discovered with Bio-Plex assay

(A) Heat map of raw signal of interactions performed with Bio-Plex. (B) Quantized heat map of analyzed

data from the Beat and Side interactions detected by the Bio-Plex. The matrix of Z scores of each Beat-Side interaction pair were divided into three categories (low, mid, high) calculated using thresholds of 80% and 90%.

Bio-Plex assay compatible with unpurified prey protein

Direct protein capture with streptavidin-coupled beads enabled us to bypass protein purification for bait proteins. We were interested to see if the assay could also be performed using unpurified prey protein, which would drastically reduce the workload involved. To test this, we performed the Bio-Plex assay using a subset of the Beat and Side families. Bait protein was expressed and captured as described above. The prey proteins were expressed in S2 cells grown in Sf-900 III, a serum-free media optimized for protein expression in insect cells. We chose serum-free media due to the fact that the multitude of extraneous proteins present in regular S2 media seem to lower the signal to noise ratio (data not shown). Using this method, we were able to find all of the expected interactions, except for Beat-Ic--Side (perhaps due to too little Beat-Ic protein captured on the beads) (Fig. 4). These results show that the Bio-Plex assay is also compatible with unpurified prey proteins.

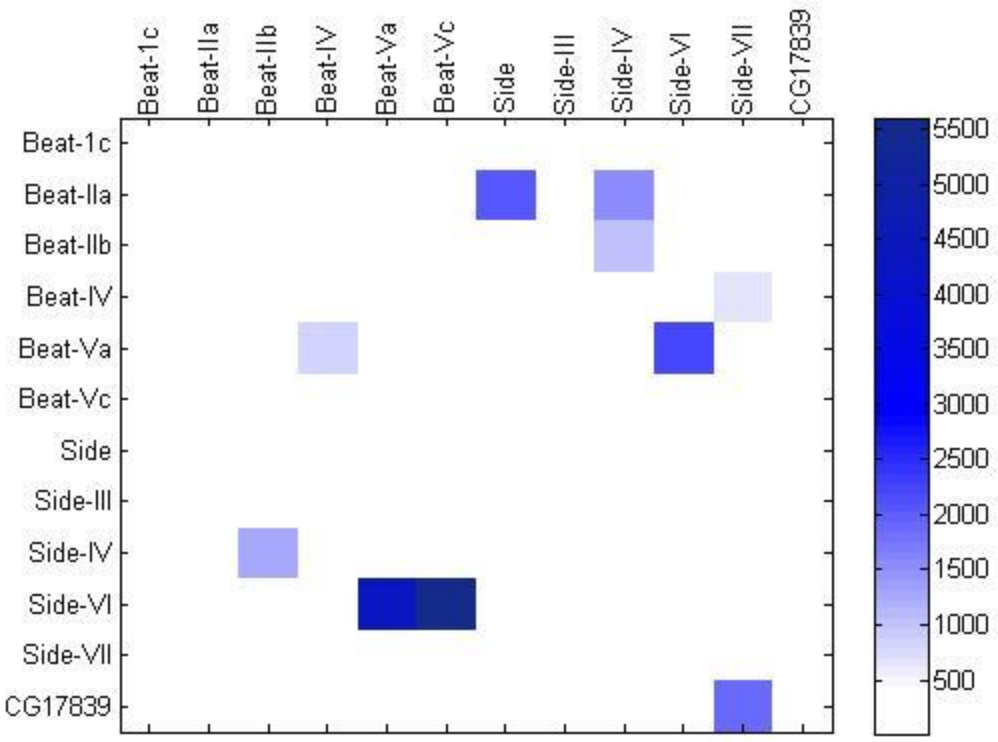

Figure 4: Heat map of raw signals of interaction between Beats and Sides performed using unpurified prey protein.

SPR verification of newly discovered Beat/Side interactions

Three new Beat/Side interactions were discovered with the Bio-Plex assay: Side-II--Beat-VI, Side--Beat-Ic, and Side-III--Beat-Ic. To verify these interactions, we measured them using surface plasmon resonance (SPR). Side-VI, Beat-Ic, and Beat-VI ectodomains were captured on Biacore chips and Side-II and Side-III were run over the chips. Interactions were observed between Side-II and Beat-VI (K_D**: 2.78**μM) and Side-III--Beat-Ic (K_D**: 63.5**μM) (Fig. 5). Binding was also observed between Side and Beat-Ic, although Side precipitation precluded the collection of a titration series.

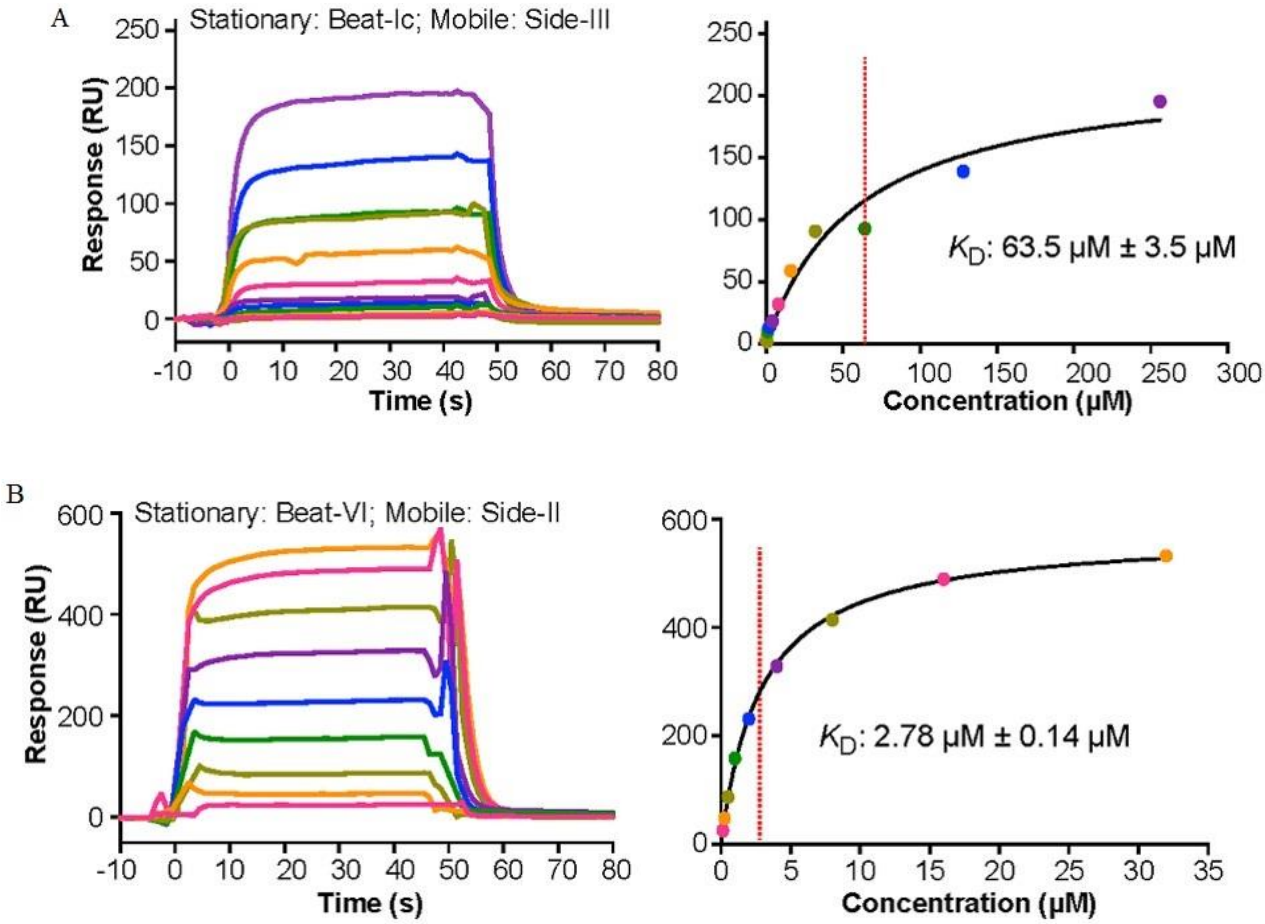

Figure 5. Surface Plasmon Resonance sensorgrams (left panels) and binding isotherms (right panels) for two Beat–Side complexes. Equilibrium binding responses are fit to Langmuir isotherms to calculate dissociation constants (K_D). Each color in the sensorgrams represents the concentration of the analyte in mobile phase. Zero time-point indicates time of analyte injection. The color scheme from the sensorgrams is preserved in the binding isotherms. (A) The interactions of Beat-Ic with Side-III and Beat-VI with Side-II (B). Beat-VI and Beat-Ic were captured on a Biacore chip, and the Sides were flowed over the chip. The ± errors represent standard error of the mean for K_D from three titration series.

Discussion

We have described a novel, high-throughput assay for detection of protein-protein interactions using the Bio-Plex system. Although many methods currently exist for this purpose, each one comes with its own advantages and disadvantages. Traditional high-throughput methods such as yeast two-hybrid are inadequate for detection of interactions

among cell surface and secreted proteins, which are often highly glycosylated and contain multiple disulfide bonds, traits which render them unfit for such cell nucleus-based assays. Y2H also suffers from relatively high false positive and false negative rates [30]. Methods such as AP-MS are also not amenable to CSSP interactions because the hydrophobic transmembrane domain of these proteins makes them difficult to solubilize and purify, while methods such as SPR are extremely sensitive, but require a large amount of protein, and therefore are not feasible as a high-throughput method.

The Bio-Plex assay enables us to circumvent many of these problems. With 100 different bead regions in the Bio-Plex® 200 system, up to 100 unique protein-protein interaction pairs can be analyzed simultaneously. Direct capture of protein with streptavidin-coupled beads allows us to bypass the purification step for bait proteins; additionally, we have shown that the assay is also compatible with unpurified prey proteins, thereby drastically reducing the workload for multiplexed screenings. The miniscule size of the beads, the ability to probe for multiple interactions simultaneously, and the small volume of the binding reactions all help reduce the amount of protein and reagents needed for the assay. We found that we were able to produce enough bait protein for our multiplexed experiments with a single 10 cm dish transfection per protein. For prey proteins, one six cm dish is sufficient to produce enough protein for our assay. The assay is also time-conserving, as its multiplex ability allows for multiple interactions to be probed in one well on a 96-well plate, and a single plate can be read in less than one hour on the Bio-Plex® 200.

We performed the Bio-Plex assay on the *Drosophila* Beat and Side protein families. Most of the proteins in these two families were orphans before Ozkan et al discovered many previously unknown interactions in their interactome generated using ELISA assays [17]. With the Bio-Plex assay, we were able to recapitulate almost all of the interactions reported in the original ECIA, as well as discover three new interactions: Beat-Ic--Side, Beat-Ic--Side-III, and

Beat-VI--Side-II. The three novel interactions were also verified by SPR. These results confirm that the Bio-Plex assay has at least comparable sensitivity compared to the ECIA.

Our findings indicate that the Bio-Plex assay is a time efficient, reagent-conserving, sensitive high-throughput method to detect protein-protein interactions.

Materials and Methods

Plasmids, cell culture and protein expression

Bait expression vectors were modified from the pECIA14 vector described in Ozkan et al [17]. An Avitag™ (Avidity) was added in between the hexahistidine and FLAG tags at the C-terminus of the vector with standard cloning procedures to make a new Gateway® (Thermo Fisher) destination vector. Entry vectors for Beats and Sides, described in Ozkan et al, were then cloned into the modified pECIA14 vector using LR Clonase® II (Thermo Fisher). Prey proteins were expressed from the pECIA2 vector described in Ozkan et al.

All proteins excepting the unpurified prey were expressed in *Drosophila* Schneider 2 cells grown in S2 media (Thermo Fisher) with 10% fetal bovine serum, 50 units/mL Penicillin and 50ug/mL streptomycin. The unpurified prey proteins were expressed in Sf-900 III media (Thermo Fisher). Proteins were transfected using Effectene (Qiagen), following manufacturer's instructions. Copper was added the day after transfection to induce expression of protein. For the pentameric prey protein, biotin was also added to the media to facilitate in vivo biotinylation. Prey proteins were purified using Ni resin following standard procedures.

Bio-Plex bead conjugation and assay

Bio-Plex Pro Magnetic COOH Beads (Bio-Rad) were coupled to streptavidin following manufacturer's instructions, and beads were blocked with 1% i-Block (Tropix) in PBS. Prey protein was then captured directly from media with streptavidin-coupled beads and pooled.

Purified (or unpurified) prey was added to the bead mix and incubated overnight at 4C. The next day, beads were washed with PBST containing 0.02% i-Block and incubated with anti-V5 antibody (Invitrogen). The beads were then washed again and incubated with goat anti-mouse IgG-PE (Santa Cruz Biotechnology). The beads were then washed, transferred into a 96-well plate and run on the Bio-Plex 200. Each reaction was run in duplicate and at least 30 beads were counted for each bead region in each well.

Data analysis

We construct an N x N matrix **X** with the rows and columns containing the N proteins in the same order. The rows denote the prey and the columns denote the bait. Thus, the ith prey interaction with jth bait is quantified by **X**(i, j), and the jth prey interaction with the ith bait is quantified by **X**(j, i). We then selected with replacement N random samples from the ith column of the matrix **X**. The process was repeated B times (B=300 was used) to obtain N B-dimensional vectors. Similarly, we selected with replacement N random samples from the ith row of **X**, and the process was repeated to obtain N B-dimensional vectors. The mean and standard deviation of each of the N rows and N columns were calculated and each component in **X** was Z-scored with respect to the column and row statistics to obtain two N x N matrices $\mathbf{X}_{zc}$ and $\mathbf{X}_{zr}$, respectively. A matrix $\mathbf{X}_{zrc}$ was formed via the element-by-element computation $\mathbf{X}_{zrc}(i,j) = (\mathbf{X}_{zr}(i,j) + \mathbf{X}_{zc}(i,j))/2$. In the scenario of both $\mathbf{X}_{zrc}(i,j)$ and $\mathbf{X}_{zrc}(j,i)$ being positive, the geometric mean of $\mathbf{X}_{zrc}(i,j)$ and $\mathbf{X}_{zrc}(j,i)$ were computed. If the geometric mean exceeded the threshold of five, then the i and j pair were labeled as an interaction. We were able to recapitulate all interactions found in the ECIA except for Side—Beat-Ia. The interaction between Side-II and Side-III was very strong in one orientation but just below our cutoff in the opposite orientation; therefore we have preserved this interaction as part of the Beat/Side network.

Protein Expression, Purification and Surface Plasmon Resonance

All Beat and Side extracellular domains with C-terminal hexahistidine tags were expressed in and secreted from *Trichoplusia ni* High Five Cells using baculoviruses. Proteins were first purified with Ni^{2+}-NTA Agarose resin, followed by size exclusion chromatography using Superdex 75 or 200 10/300 columns (GE Healthcare). For capturing on Surface Plasmon Resonance chips, Beat-Ic and Beat-VI expression constructs also included a biotin acceptor peptide sequence, which was used to biotinylate using *E. coli* BirA biotin ligase, and allowed proteins to be captured on SA (streptavidin) Biacore chips (GE Healthcare). Side-II and Side-III were titrated in the mobile phase over the SA chips.

Beat-Ic and Beat-VI expression constructs included complete ectodomains. Due to problems with expression and/or purification for full-ectodomain constructs of Side, Side-II, and Side-III, shorter fragments of these Side ectodomains were used for SPR, based on the knowledge that the first immunoglobulin domains of Sides are sufficient for Beat-Side interactions (data not published). The following constructs were used during SPR experiments: N-terminal two Ig domains of Sidestep and N-terminal single-Ig domains of Side-II and Side-III.

Surface Plasmon Resonance (SPR) experiments for Beat-Ic and Beat-VI against Side-II and Side-III were performed on a Biacore 3000. Unless noted, all SPR binding measurements are done in HBSp+ (GE Healthcare), which includes 10 mM HEPES pH 7.2, 150 mM NaCl, and 0.05% surfactant Polysorbate 20. To prevent non-specific binding to Biacore chip surfaces Side-II and Side-III binding was performed in the buffer HBSp+ and 1% (w/v) bovine serum albumin (BSA).

Binding between Sidestep (mobile phase) and Beat-Ic (stationary phase) could also be observed, but precipitation of Sidestep prevented us from collecting a titration series.

References

1. Tarassov, K., et al., *An in Vivo Map of the Yeast Protein Interactome.* Science, 2008. **320**(5882): p. 1465-1470.

2. Li, S., et al., *A Map of the Interactome Network of the Metazoan C. elegans*. Science, 2004. **303**(5657): p. 540-543.

3. Simonis, N., et al., *Empirically controlled mapping of the Caenorhabditis elegans protein-protein interactome network*. Nat Meth, 2009. **6**(1): p. 47-54.

4. Guruharsha, K.G., et al., *A Protein Complex Network of Drosophila melanogaster.* Cell, 2011. **147**(3): p. 690-703.

5. Giot, L., et al., *A Protein Interaction Map of Drosophila melanogaster*. Science, 2003. **302**(5651): p. 1727-1736.

6. Nooren, I.M.A. and J.M. Thornton, *Diversity of protein–protein interactions.* The EMBO Journal, 2003. **22**(14): p. 3486-3492.

7. Bushell, K.M., et al., *Large-scale screening for novel low-affinity extracellular protein interactions.* Genome Res, 2008. **18**.

8. Clark, H.F., et al., *The Secreted Protein Discovery Initiative (SPDI), a Large-Scale Effort to Identify Novel Human Secreted and Transmembrane Proteins: A Bioinformatics Assessment*. Genome Research, 2003. **13**(10): p. 2265-2270.

9. Braun, P., et al., *An experimentally derived confidence score for binary protein-protein interactions.* Nat Meth, 2009. **6**(1): p. 91-97.

10. Miller, J.P., et al., *Large-scale identification of yeast integral membrane protein interactions.* Proceedings of the National Academy of Sciences of the United States of America, 2005. **102**(34): p. 12123-12128.

11. Wright, Gavin J., et al., *High-throughput identification of transient extracellular protein interactions.* Biochemical Society Transactions, 2010. **38**(4): p. 919-922.

12. Anton van der Merwe, P. and A. Neil Barclay, *Transient intercellular adhesion: the importance of weak protein-protein interactions.* Trends in Biochemical Sciences, 1994. **19**(9): p. 354-358.

13. Wright, G.J., *Signal initiation in biological systems: the properties and detection of transient extracellular protein interactions †This article is part of a Molecular BioSystems themed issue on Computational and Systems Biology.* Molecular Biosystems, 2009. **5**(12): p. 1405-1412.

14. Wojtowicz, W.M., et al., *A Vast Repertoire of Dscam Binding Specificities Arises from Modular Interactions of Variable Ig Domains.* Cell, 2007. **130**(6): p. 1134-1145.

15. Söllner, C. and G.J. Wright, *A cell surface interaction network of neural leucine-rich repeat receptors.* Genome Biology, 2009. **10**(9): p. R99.

16. Ramani, S.R., et al., *A secreted protein microarray platform for extracellular protein interaction discovery.* Analytical Biochemistry, 2012. **420**(2): p. 127-138.

17. Özkan, E., et al., *An Extracellular Interactome of Immunoglobulin and LRR Proteins Reveals Receptor-Ligand Networks.* Cell, 2013. **154**(1): p. 228-239.

18. Voulgaraki, D., et al., *Multivalent recombinant proteins for probing functions of leucocyte surface proteins such as the CD200 receptor.* Immunology, 2005. **115**(3): p. 337-346.

19. Ashraf, S.S., et al., *A novel multi-affinity tag system to produce high levels of soluble and biotinylated proteins in Escherichia coli.* Protein Expression and Purification, 2004. **33**(2): p. 238-245.

20. Sung, K., et al., *A Novel Method for Producing Mono-biotinylated, Biologically Active Neurotrophic Factors: An Essential Reagent for Single Molecule Study of Axonal Transport.* Journal of neuroscience methods, 2011. **200**(2): p. 121-128.

21. Wang, Q., R.T. Wagner, and A.J. Cooney, *Regulatable in vivo biotinylation expression system in mouse embryonic stem cells.* PLoS One, 2013. **8**(5): p. e63532.

22. Tykvart, J., et al., *Efficient and versatile one-step affinity purification of in vivo biotinylated proteins: Expression, characterization and structure analysis of recombinant human Glutamate Carboxypeptidase II.* Protein expression and purification, 2012. **82**(1): p. 106-115.

23. Hendrickson, W.A., et al., *Crystal structure of core streptavidin determined from multiwavelength anomalous diffraction of synchrotron radiation.* Proceedings of the National Academy of Sciences of the United States of America, 1989. **86**(7): p. 2190-2194.

24. Pipes, G.C.T., et al., *The Beat generation: a multigene family encoding IgSF proteins related to the Beat axon guidance molecule in Drosophila*. Development, 2001. **128**(22): p. 4545-4552.

25. Fambrough, D. and C.S. Goodman, *The Drosophila beaten path Gene Encodes a Novel Secreted Protein That Regulates Defasciculation at Motor Axon Choice Points.* Cell, 1996. **87**(6): p. 1049-1058.

26. Sink, H., et al., *sidestep Encodes a Target-Derived Attractant Essential for Motor Axon Guidance in Drosophila.* Cell, 2001. **105**(1): p. 57-67.

27. Siebert, M., et al., *Drosophila motor axons recognize and follow a Sidestep-labeled substrate pathway to reach their target fields.* Genes & Development, 2009. **23**(9): p. 1052-1062.

28. Zinn, K., *Choosing the road less traveled by: a ligand-receptor system that controls target recognition by Drosophila motor axons.* Genes Dev, 2009. **23**(9): p. 1042-5.

29. Aberle, H., *Searching for guidance cues Follow the Sidestep trail.* Fly, 2009. **3**(4): p. 270-273.

30. Deane, C.M., et al., *Protein Interactions: Two Methods for Assessment of the Reliability of High Throughput Observations.* Molecular & Cellular Proteomics, 2002. **1**(5): p. 349-356.

Chapter 3

Expression Diversification and Invariant Specificity Determine the Complexity of Interactions of Beat Receptors with Their Side Ligands

Introduction

Ligand-receptor interactions are fundamental to intercellular communication and the integration of information from the extracellular environment. The requirement for specificity of cell surface interactions in multicellular organisms has favored the proliferation of families of specialized molecules capable of high specificity homo- and heterophilic interactions. During nervous system development such molecules play key roles, as neuronal projections must extend often very long distances to find and synapse with the appropriate targets. The trajectory of pathfinding axons is controlled by the contribution and modulation of signals from attractive, adhesive, and repulsive interactions [1]. The *beaten-path* (*beat-Ia*) and *sidestep* (*side)* genes encode a membrane associated receptor ligand pair that has been shown to be crucial for the guidance of motor axons in the developing *Drosophila melanogaster* embryo [2-6]. The direct interaction between these molecules and the complex they are a part of allows Beat-Ia expressing motor growth cones to contact and navigate over substrates that dynamically express Side [6, 7]. Beat-Ia belongs to a larger sub-family of proteins consisting of fourteen members in *Drosophila* [3] while eight Side related genes have also been identified [7-9] and shown to be able to bind Beat receptors in vitro [10].

Gene duplication, a key phenomenon in the expansion of gene families, provides an opportunity for the fine-tuning or innovation of protein interactions and functions [11]. In

the case of duplicated genes encoding ligands and receptors, while one gene copy can maintain specific interactions with its ancestral binding partners, the other paralog, free of selection pressures due to its genetic redundancy with its sister copy, could evolve differing spatiotemporal expression patterns. The divergence between the two copies of a duplicated gene could allow more diverse and independent responses to binding partners that are common to both paralogs. Indeed, the duplication of genes encoding receptors or ligands with multiple interactions can be followed by sub-functionalization, with a total or partial partitioning of the ancestral interactions between both gene copies. Relaxed constraints due to functional redundancy between duplicated genes could also lead to the exploration of new functions by one of the gene copies. In these ways, members of one family of molecules may establish an interaction network with another family of molecules that each present differing promiscuities and specificities for their interactors.

Sides and *beats* have undergone a number of duplication events and we hypothesize that both families of interacting proteins have evolutionarily co-diversified resulting in an increased complexity of the insect nervous systems. To demonstrate this hypothesis, in this work we show that the Side family of proteins contain an invariable extracellular architecture of five immunoglobulin domains followed by a Fibronectin type III domain and this family has originated through successive gene duplication events pre-dating the origin of Drosophilids. A detailed analysis of the evolutionary diversification of interaction profiles and expression patterns in individual motoneurons shows, for the first time, the link between sizes of protein families and the functional and regulatory specialization of Beat receptors. Gene duplication has led to functional diversification followed by a fine-tuning of Sides-Beat specific interactions in which co-adaptation dynamics has originated a strong co-evolutionary relationship between members of both families. Indeed, we show that the Beat-V subgroup interacts specifically with Side-VI with high affinity to mediate the motor-axon guidance and

targeting in vivo in the *Drosophila* embryo. Beat and Side proteins are two large protein families engaging in ligand-receptor interactions in vivo during development and their co-evolutionary diversification has been key to the developmental complexity of the insect nervous system.

Results

Side belongs to larger family of Side proteins predating Drosophilid speciation

The *beaten-path* (*beat-Ia*) and *sidestep* (*side*) genes and their protein products interact genetically and physically to facilitate motor axon guidance in the developing embryo [2-6, 12]. The Beat-Ia and Side interaction has been characterized in vivo as an attractive, adhesive interaction where Beat-Ia expressing motor axon growth cones advance along a labeled pathway of substrates, including muscle primordia and sensory neurons, that transiently express Side [6]. A number of the additional Beat genes have been shown to be expressed in the embryonic CNS [3], while Side has been suggested to belong to a family of paralogous (duplicated) genes [7-10]. Side related proteins have been described as transmembrane proteins containing between four and five immunoglobulin (IG) domains followed in some instances by fibronectin type III (FNIII) domain in their extracellular region [4, 7]. An exhaustive analysis using SMART [13], HMMER [14], and DOUT-finder [15] to identify outlier homologs of structural domains reveals that the Side family of paralogous genes has an invariant extracellular domain architecture likely composed of five IG domains followed by an FNIII domain (Fig. 1A). In some cases their sequence has diverged substantially from the described consensus for these domains, making their identification difficult through standard searches.

In addition to the protein domain-based composition, phylogenetic inferences provide evidence for a cohesive family of Sides proteins (Fig. 1B). We refer to Sidestep as Side, and have designated numbers to the other seven Side paralogs based on their evolutionary distance from Side. All Side paralogs seem to present similar or comparable levels of inter-species (intra-paralog) divergence, indicating that different Side paralogs have undergone similar selective constraints. The presence of Side paralogs in most of the 12 sequenced Drosophilids, and the presence of orthologs of some of these paralogs in the mosquito, *Anopheles gambiae*, clearly indicate the origin of the Side family through successive duplication events that pre-dated Drosophilid speciation. We could not identify orthologs in all 12 Drosophilids for all Sides likely due to incomplete genomic sequence rather than stochastic loss of some non-functionalized paralogs after gene duplication, as predicted by Ohno's classic theory [11].

However, the missing orthologs within Sides clusters are likely due to limitations of methods to identify them because (a) Sides paralog clusters containing low numbers of orthologs present similar inter-species divergence levels as those containing high number of orthologs, hence equal selective constraints; (b) evolutionary instability of functionally redundant gene copies, which would lead to the non-functionalization and erosion of redundant paralogs, is not a plausible evolutionary explanation to the missing orthologs since the large inter-Sides divergence levels imply that paralogs diverged functionally after gene duplication, and thus they were not functionally redundant; and c) the loss of redundant paralogs is expected soon after duplication [16], likely pre-dating speciation. Therefore, the most likely scenario given our phylogenetic trees is that Sides' ancestral gene duplicated successively and was followed by a rapid sequence and functional divergence pre-dating Drosophilid speciation. Indeed, rooted trees for the Side family show a dynamic history of gene duplication and divergence, with highly asymmetric clusters of duplicates resulting

from faster evolution of one gene copy compared to its sister one, indicating possible functional divergence and specialization after gene duplication. Our rooted phylogeny of the Side paralogs differs from a previous unrooted one [7]. The low bootstrap support values (P < 60%) for some of the internal tree branches indicate rapid successive duplication events. The long branches post-dating duplications but pre-dating speciation support enormous divergence between the duplicates at the sequence, and very probably functional levels followed by strong purifying selection after speciation.

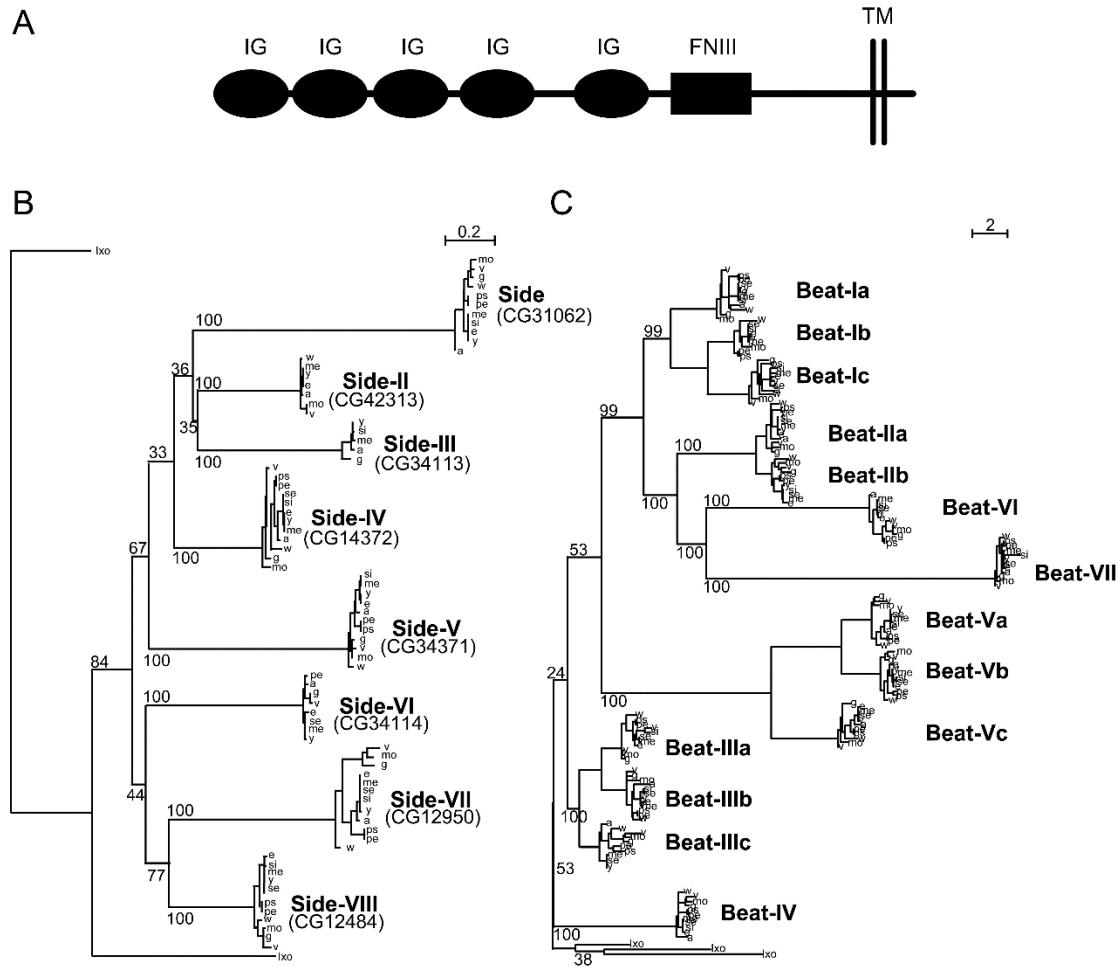

Figure 1: Phylogenetic analysis and interactome of the Beaten-Path and Sidestep paralogs

(A) Extracellular architecture of the Side family of related proteins. Detailed ClustalW alignment of individual domains and conservation in figure S1 (IG, immunoglobulin; FNIII, Fibronectin type III; TM, transmembrane domain). (B) Phylogeny of the Side family of related proteins rooted against similar Immunoglobulin superfamily proteins predicted in the tick, *Ixoides scapularis* (Ixo) that form a distinct outgroup. Names are assigned to the paralogs on the basis of their evolutionary distance from Sidestep and their CG flybase identifiers are in parentheses. (C) Phylogeny of the Beat family of receptors rooted against *Ixoides scapularis* Beats. Beat-VII and Beat-VI share a more recent ancestor than previously described [40].

Interaction profiles for Sides and Beats indicate functional and regulatory specialization after gene duplication

A phylogenetic study was also carried out to establish the phylogenetic extent and architecture of the *beat* family (Fig. 1C). The *beat* family was previously designated into clustered groups. More recent tandem duplications have left groups of *beat* genes in tandem arrays on chromosome arm 2L (*beat-Ia/b/c* and *beat-IIIa/b*) and 3R (all other *beat* genes). The *beat* family has a more complex architecture than the *side* family owing in no small part to recent tandem duplication and retention of the clustered members –*beat-Ia/Ib/Ic, beat-IIa/IIb,* and *beat-Va/Vb/Vc*. Our phylogenies show that *beat-VI* and *beat-VII* are more closely related than previously thought [3]. While divergence rates along the *beat* family phylogeny are highly asymmetric following the earliest duplications, groups of *beats* within each of the clusters of paralogs present similar divergence levels (i.e., Beat-IIa and Beat-IIb present similar rates of evolution). This observation suggests that *beats* have undergone two levels of specialization: functional specialization post-dating duplication and emergence of the seven major *beat* branches followed by regulatory specialization of the four minor *beat* clusters.

Interacting proteins usually exercise reciprocal natural selection on one another, so that changes in one protein induce changes in the other interacting one to co-adapt. These co-adaptations lead to signatures of co-evolution, generally identified using molecular phylogenetic approaches. *Beats* and *sides* have undergone a number of duplication events [3, 8]. Following Ohno's theory [11], gene duplication is likely to be followed by non-functionalization of one copy. However, genes remaining in duplicate are those that have either diverged at the functional, expression, or functional and expression levels.

The recurrent preservation of duplication copies of *sides* and *beats* suggest the specialization of the different Side-Beat interactions. However, the asymmetry in the architecture of both families--that is, the unequal duplication frequency--is quite striking and

supports interactions of one Side to many Beats. Sides and Beats have undergone a number of duplication events, and we sought to investigate whether their evolutionary history correlated with interacting partners identified in our Extracellular Interactome of Immunoglobulin superfamily proteins [10] and a dedicated Bio-Plex assay (Fig. 1D), using. Importantly, the interaction profiles between Sides and Beats indicate functional specialization of Sides to interact with specific Beat clusters. A remarkable observation is the phylogenetic mirroring between Sides and Beats when we take their interaction profiles into account: Sides closer to the root of the tree interact with Beats also close to the root of the tree and vice versa. For example, Side-VII interacts with Beat-IV, both close to the root of the tree, while Side-VI interacts Beat-V cluster, both of which are at proportionally equivalent distances from the root of their respective tree. This phylogenetic mirroring of the interaction profiles attests to the evolution of Sides and Beats complexity through a specialization and co-adaptation dynamic.

The expression patterns of the *side* family of genes suggest a role as ligands for pathfinding receptors

Side protein expression presents spatial and temporal plasticity [41, 42]. At early stages (stage 12) it is expressed in cells in a belt-like pattern within the CNS around the midline and slightly later in a cluster of cells with a triangular pattern followed by the inter-segmental nerve (ISN) on its way to the muscle field. At later stages Side is expressed in sensory afferents, where it is downregulated following contact with Beat-Ia expressing growth cones, and expression starts in the muscle fibers, thus labeling all substrates followed by the ISN towards its peripheral targets [42]. We reasoned that expression of *side* paralogs along or at an important guidepost or choice points in these nerve tracts would be a good preliminary indicator of other potential Beat-Side interactions. Therefore, we examined the embryonic expression of *side-II, side-III, side-VI, side-VII*, and *side-VIII* by fluorescence in situ mRNA

hybridization and labeled all motor axons with the monoclonal anti-fasciclin-II antibody, ID4, to assess the coordinates of their expression relative to wild-type motor axon trajectories.

With the exception of *side-VIII*, the most distant relative of *sidestep* studied, which shows expression largely restricted to specific cells within the CNS including RP1, 3, 4, 5, and the aCC, pCC, and RP2, the other *side* genes exhibit broad patterns of expression, often seen to surround or coincide with the path of motor nerve trajectories (Fig. 2). *side-II* is transcribed broadly in the CNS and to a lesser extent in the developing musculature (Fig. 2A). *side-III* is initially expressed at high levels in the mesoderm and muscle primordia and broad transcription in the CNS increases as embryonic development progresses. By stage 14 peripheral *side-III* expression is strongest in the developing trachea and in stripes in the ectoderm along the parasegmental furrows (Fig. 2B, K). The developing trachea is a known intermediate target of the ISN and certain sensory neurons [43, 44]. *side-VII* shows pan-neural expression in the CNS and similarly to *side-III* it is transcribed in the trachea and in epidermal stripes (Fig. 2C, K). The pattern of expression of *side-VI* is particularly compelling. After stage 14-15 it is expressed in the musculature, particularly in the medial external musculature targeted by a branch of the segmental nerve (SNa) and in the ventral internal muscles targeted by the ISNb, especially muscle 12, when the ISNb establishes its branches between the ventral muscles during stage 16 (Fig. 2E, J, K). *side-VI* is also transcribed in cells whose surfaces are explored by the ISN tip such as the dorsal cluster of Lim3 positive sensory neurons that fasciculate with the ISN (Fig. 2F, K), and in a "persistent twist expressing cell" (PT cell) which coincides with the first branch point of the ISN (FB) within the dorsal musculature [45] (Fig. 2G, K). *side-VI* is also expressed in certain targets of the transverse nerve (TN) that are known to be essential for its guidance, including the lateral bi-dendritic neuron (LBD) (Fig. 2H, K) and the dorsal median cell (DMC) [46, 47] (Fig. 2I, K).

Overall, the broader expression patterns of the *side* genes examined are suggestive of a role as guidance cues or as components of broadly utilized co-receptor/ligand complexes. In particular, the dynamic nature of *side-VI* expression and the fact that it is expressed at intermediate and final targets of the ISN, ISNb, SNa, and TN suggests that it may play a role in guiding motor axons towards their targets through receptors expressed on these nerves. The differential expression of Sides paralogs also suggest a divergence in expression and, very possibly, their functional specialization after duplication in guiding motor axons to different sets of targets during specific developmental stages.

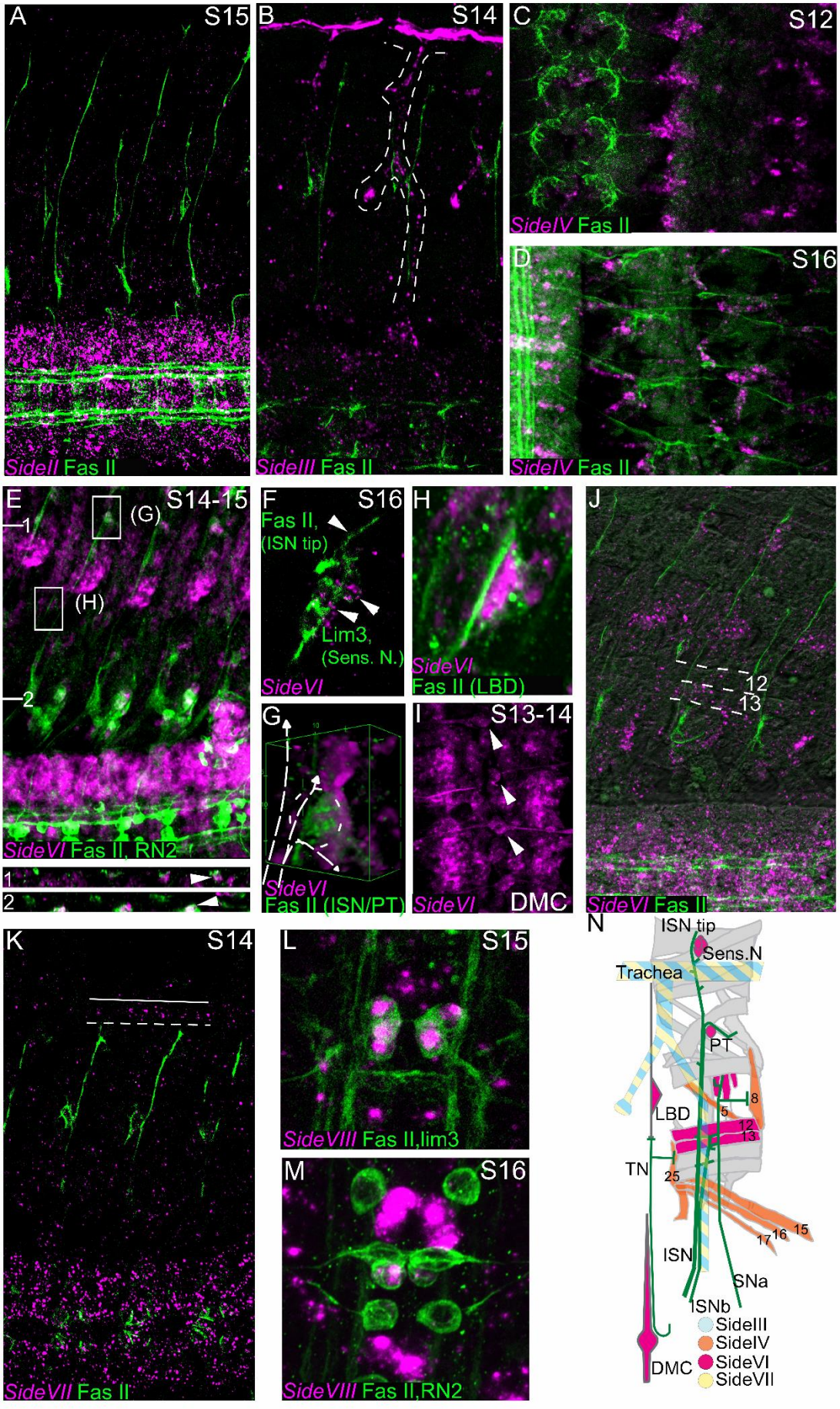
A
S15
SideII Fas II
B
S14
SideIII Fas II
C
S12
SideIV Fas II
D
S16
SideIV Fas II
E
S14-15
(G)
(H)
1
2
SideVI Fas II, RN2
1
2
F
S16
Fas II,
(ISN tip)
Lim3,
(Sens. N.)
SideVI
H
SideVI
Fas II (LBD)
G
SideVI
Fas II (ISN/PT)
I
S13-14
SideVI
DMC
J
12
13
SideVI Fas II
K
S14
SideVII Fas II
L
S15
SideVIII Fas II,lim3
M
S16
SideVIII Fas II,RN2
N
ISN tip
Sens.N
Trachea
PT
LBD
5
8
12
13
TN
25
15
16
17
ISN
SNa
ISNb
SideIII
SideIV
SideVI
SideVII
DMC

Figure 2: Embryonic expression of the *side* genes suggests roles as chemotropic ligands. Fluorescent in situ hybridization (magenta) of s*ide-II, side-III, side-VI, side-VII, and side-VIII* genes in fillet preparations. All preparations are co-stained with anti-Fasciclin II antibody to reveal all motor nerves (green). (A) *side-II* is predominantly expressed in the CNS, where it has an increasingly broad expression pattern as development progresses. (B) *side-III* expression pattern in a stage 14 embryo in the developing trachea (dashed line). (C) *side-VII* expression in a S14 embryo is broad in the CNS and in the trachea (outlined). *side-VIII* expression at stages 15-16 in RP 1, 3, 4, 5 motor neurons co-stained for lim3-taumyc (D) and the pCC interneuron co-stained RN2Gal4::UAS-tau-LacZ (D'). (E) Expression of *side-VI* at stage 14-15 co-stained for RN2Gal4::UAS-tau-LacZ. *side-VI* is broadly expressed in the CNS and in specific tissues in the periphery. XZ sections are indicated and represented underneath the main panel and magnifications of selected areas (G, H) are presented in individual panels. Orthogonal views show a cross section of a dorsal set of sensory neurons (1) and the junction of the ISN at its first branch, FB (2). The location of the ISN is marked with an arrowhead. (F) In a stage 16 embryo the ISN tip explores a group of *side-VI* expressing dorsal sensory neurons. (G) 3D projection of the ISN FB region where *side-VI* is expressed at high levels in the PT cell. The path of the ISN is overlaid with a dashed line.
(H) The lateral bidendric neuron (LBD), a synaptic target of the transverse nerve (TN) expresses high levels of *side-VI*. I) *side-VI* is expressed in the dorsal median cell (DMC, arrowheads). (J) *side-VI* expression in ventral muscles in a stage 16 embryo (muscles 12 and 13 are outlined). (K) Synopsis of *side-III, VI* and *VII* expression in the periphery. Anterior is left and the ventral CNS is down in all panels except D, D' and J where anterior is up.

In addition to embryos, we also studied the expression patterns of Beat-Va and Side-VI in CNS, motoneurons and muscles of *Drosophila* 3rd instar larvae. To do this, we used Side-VI-GAL4 and Beat-Va-GAL4 lines driving GFP. We found that all NMJs are labeled by reporters driven by both the Beat-Va and Side-VI GAL4 drivers, indicating that both genes are expressed in all motor neurons in larvae (Fig. 3). We also observed expression in subsets of sensory neurons and the ventral nerve cord (data not shown). Muscle expression is not prominent, but we cannot rule out the possibility that muscle fibers express the genes at low levels.

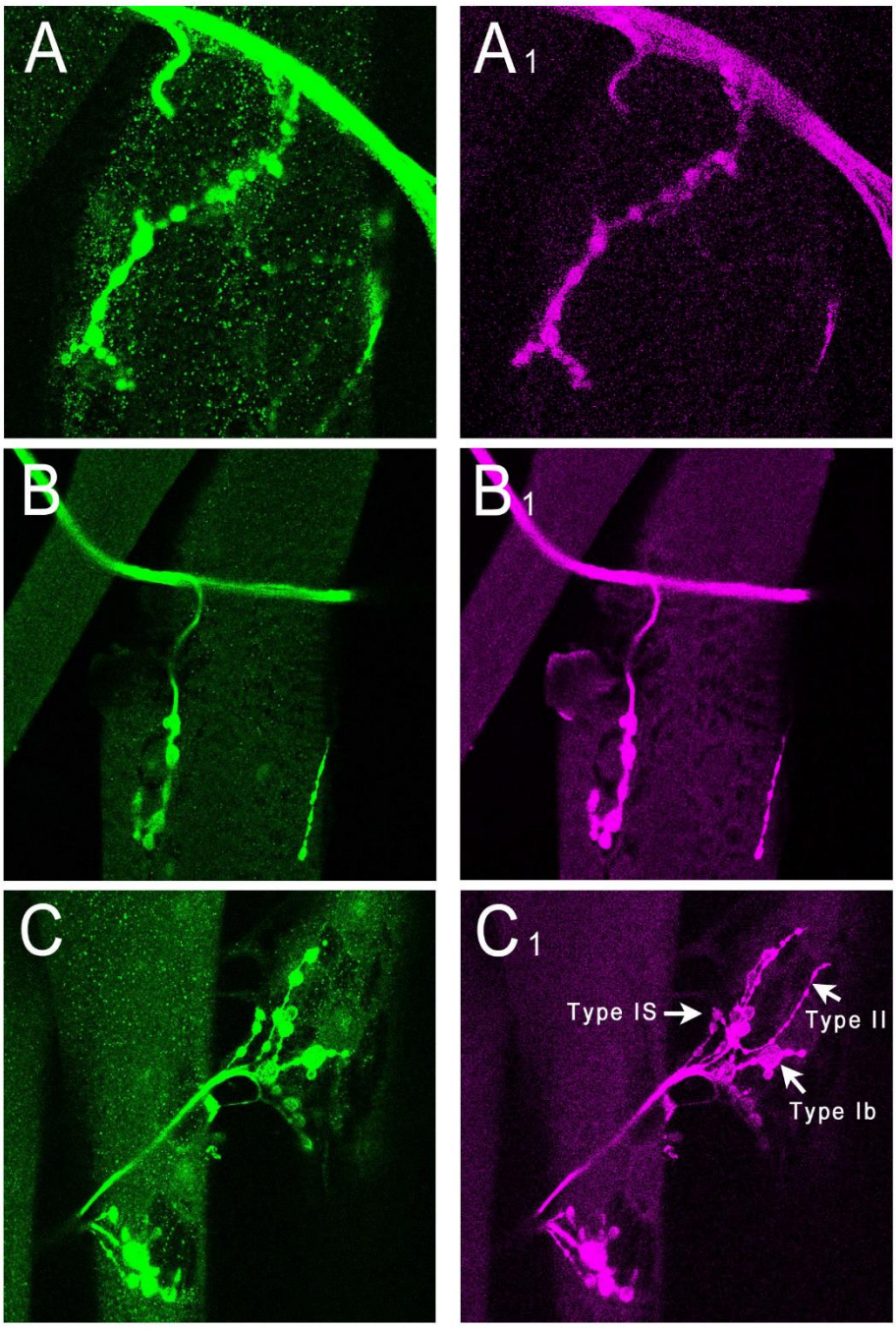

Figure 3: Larval expression of Beat-Va>GFP and Side-VI>GFP. (A, A_1) Beat-Va expression at muscle 4 of 3rd instar larva. Green is stained with anti-GFP and magenta is stained with anti-HRP. (B, B_1) Side-VI expression at muscle 4 of larva. (C, C_1) Side-VI expression at muscles 12, 13 of larva.

Embryonic expression patterns in motor neurons have diverged within the Beat-I and Beat-V groups

We focused on the *beat* family members expressed at appreciable levels in the CNS [40] and analyzed if the expression of clustered paralogs had diverged following duplication by evaluating their expression in single motor neurons. We performed in situ mRNA hybridization combined with simultaneous immunohistochemistry and confocal imaging with two marker lines (RN2-Gal4 and Lim3A-tau-myc, [48, 49]) to specifically identify pioneer neurons of the dorsal bound ISN (aCC and RP2) [49] or of the ventral bound ISNb (RP1, 3, 4 and 5). While the *beat* genes are transcribed within motor neurons in the CNS, there is considerable difference between the expression patterns of individual members of the Beat-I and Beat-V clusters (Fig. 4).

Within the *beat-I* subfamily, *beat-Ia* is transcribed in both the aCC and RP2 motoneurons of the ISN (Fig. 4A, F), where its transcription is dependent on *eve* ([50] and data not shown) and RP 1, 3, 4, and 5 ([40] and data not shown); *beat-Ib* and *beat-Ic* do not appear to be transcribed in RP1, 3, 4, and 5 motor neurons of the ISNb (Fig. 4B and 4D respectively) but both are expressed in the aCC and RP2 motoneurons of the ISN although *beat-Ib* levels are relatively low (Fig. 4C for *beat-Ib* and E for *beat-Ic*). Both *beat-Va* and *beat-Vb* are differentially expressed in ISNb and ISN motoneurons almost in a mutually exclusive manner. *Beat-Va* is absent from RP1, 3, 4, and 5 (Fig. 4G), but is expressed at high levels in the RP2 and at lower levels in the aCC (Fig. 4H, F). On the other hand *beat-Vb* is transcribed at very high levels in the RP1, 3, 4, and 5 (Fig. 4I, F), while expression in the aCC and RP2 motoneurons is considerably weaker and only visible at a late stage embryos (stage 16), at which point expression has become weaker within the CNS (Fig. 4J, K). The fact that *beat-Va* and *beat-Vb* are expressed to different degrees in pioneers of two different motor nerve tracts suggests possible roles as chemotropic receptors in the development of these two nerve tracts.

In addition, our results show that embryonic expression patterns within the CNS have diversified between clustered *beat* paralogs within the *beat-I* and *beat-V* groups.

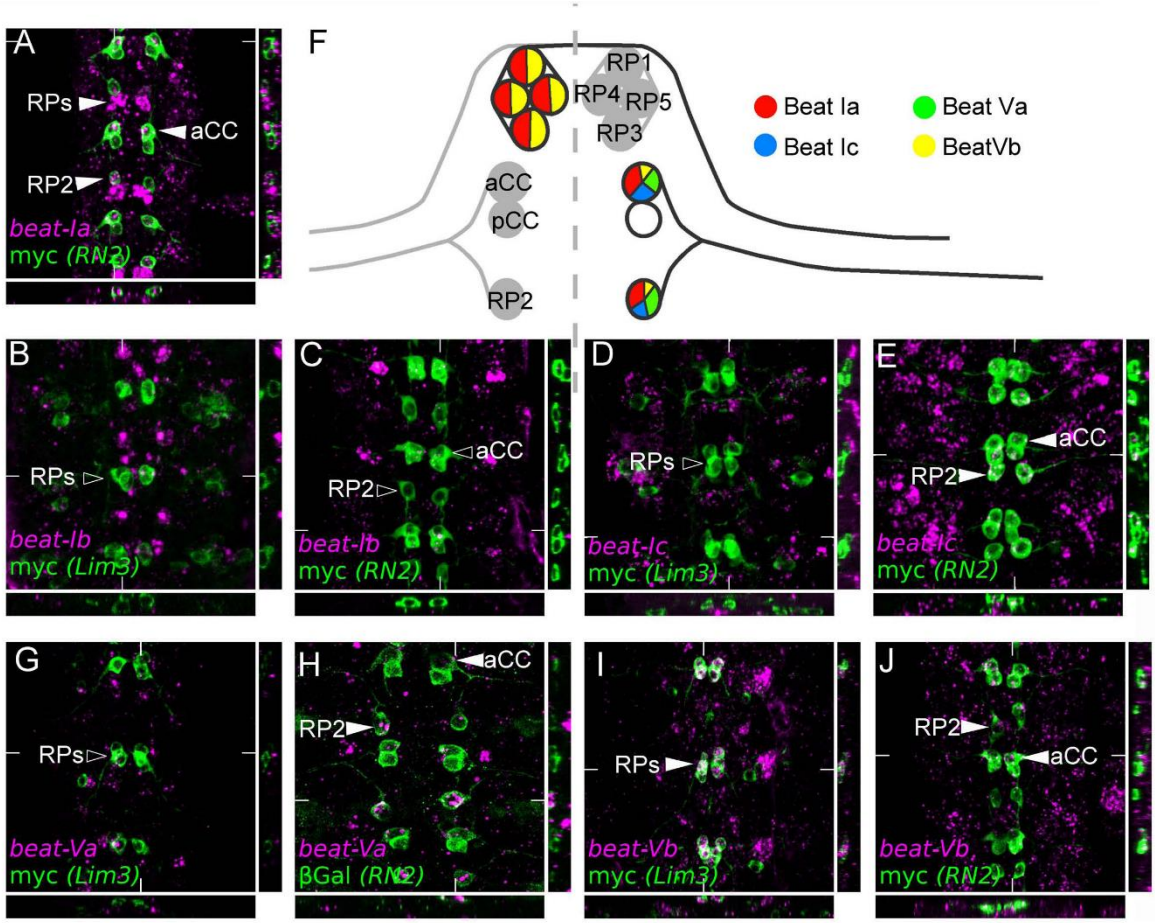

Figure 4: Embryonic expression of *beat-I* and *beat-V* subgroups in motor neurons indicates regulatory divergence. In situ mRNA hybridization of the *Beat-I* group and *Beat-V* group of genes (magenta). Individual motor neurons are marked (green) with anti-myc in a *Lim3A-tau-myc* (*Lim3*) line and anti-myc or anti-βGal in *RN2-Gal4::UAS-tau-myc-eGFP* and *RN2-Gal4::UAS-LacZ* (*RN2*) to reveal RP1, 3, 4, 5, or aCC and RP2 cells respectively. (A) *beat-Ia* is transcribed in the ISN pioneer motor neurons aCC and RP2 and RPs 1, 3, 4, 5 (arrowheads). (B) *beat-Ib* is not expressed at appreciable levels in the ISNb motor neurons, RP1, 3, 4, or 5 nor the other Lim3 neurons. (C) *beat-Ib* is not transcribed at observable levels in the aCC or RP2 motor neurons. (D) *beat-Ic* is not expressed transcribed in the ISNb motor neurons marked in *Lim3* embryos but is expressed to some in the aCC and RP2 motor neurons of the ISN (E). (G) *beat-Va* is not expressed at in the RP1, 3, 4, or 5 motor

neurons but is expressed in the aCC and RP2 motor neurons, clearly showing higher levels in the RP2 motor neuron (H). (I) *beat-Vb* is transcribed at high levels in the RP1, 3, 4, and 5 motor neurons and at low levels in the aCC and RP2 (J). All embryos are dissected to expose the CNS. Anterior is up in all images, with the ventral midline in the center. Coordinates of orthogonal slices are indicated on main panels and XY and XZ cuts are represented to the right and bottom of each panel respectively. (F) Expression profiles of Beat-I and Beat-V group of genes in dorsal and ventral projecting motor neurons.

side-VI and the *beat-V* mutants share motor axon pathfinding defects

The complementary expression patterns of the *side-VI* and *beat-Vs* genes indicate that they may be required during motor axon guidance. Therefore, to test whether our data reflected a functional requirement in vivo for the *beat-Vs* and *side-VI* during motor axon guidance we assessed whether removal of the *beat-V* or *side-VI* genes would result in similar motor axon guidance defects. As the *beat-Vs* are found in a tight tandem array on chromosome 3R the three Beat-V receptors were removed together with a deficiency (*Df(3R)Exel7318*, henceforth *Df-beat-Vs*). To eliminate *side-VI* we also used a deficiency line (*Df(3R)Exel7306*). This *side-VI* deficiency line was crossed to a *side*-VI MiMIC line *side-VI*^{MiMIC38121}. Two motor axon guidance phenotypes were noted in common in the transverse nerve (TN), intersegmental nerve (ISN), and the ISNb (Fig. 5). For Side-VI/Df, we observed low-penetrance ISNb phenotypes in early stage 17 embryos (16% (n=227 hemisegments) vs. 6% (n=225) in controls; $p=2.53e^{-7}$). In some hemisegments, the ISNb had not extended to muscle 12 at this stage, but terminates on muscle 13, whereas in other hemisegments, the ISNb grew over to the ISN or TN from muscle 13 and appeared to fuse with one of these pathways. Also in some of these hemisegments, muscle 12 appeared to be innervated by a branch emerging from the ISN or TN (Fig. 5).

In *Df-beat-V* embryos, we observed phenotypes resembling those in *side-VI* mutants, and with a similar penetrance (20%; n=141). However, since this Df line also takes out parts

of other nearby genes, we cannot be certain that the observed phenotypes are due to loss of the *beat-V* genes.

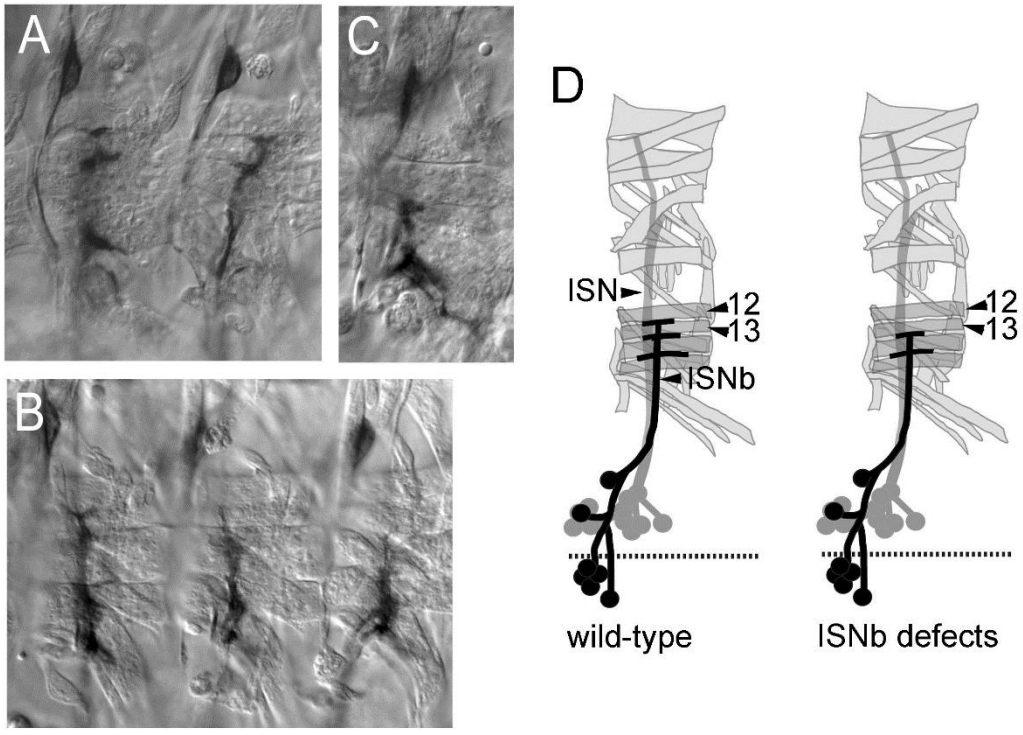

Figure 5: DAB staining of *beat-V* and *side-VI* mutants. (A and C) *side-VI* mutant embryos shows failure of muscle 12 innervation of the ISNb. (B) Wild-type embryos.

Side-VI interacts with Beat-V paralogs in vitro and in vivo

The complementary embryonic mRNA expression pattern of *side-VI* and the *beat-Vs* together with their overlapping motor axon phenotypes indicate that Side-VI behaves as a guidance cue for several motor nerves. We reasoned that we might be able to detect an interaction in vivo between Side-VI and its putative receptors in axonal membranes as has been previously shown for other guidance molecules in *Drosophila* [10, 25, 26]. To test this hypothesis we fused the ectodomain-encoding region of the Side-VI cDNA to human

placental alkaline phosphatase (PLAP) tag [27] to create a soluble affinity probe, Side-VI-AP and determined which embryonic tissues might express binding partners for Side-VI. While Side-VI-AP also binds to axons broadly within the neuropil of the CNS (Fig. 6A & B), interestingly, it is seen to specifically bind to axons of the ISNb, ISN, SN (Fig. 6A, B) and the TN (Fig. 6C, D). Given that Side-VI-AP is found to bind to the motor nerves where both

Beat-I and the Beat-V subgroups of receptors are expressed we wondered if Side-VI could interact directly with them. Therefore, we tested whether the soluble Side-VI-AP was capable of binding to Beat receptors expressed on the membrane of *Drosophila* S2 cells. We found that both Beat-Va and Beat-Vb bound Side-V-AP, while Beat-Ia did not.

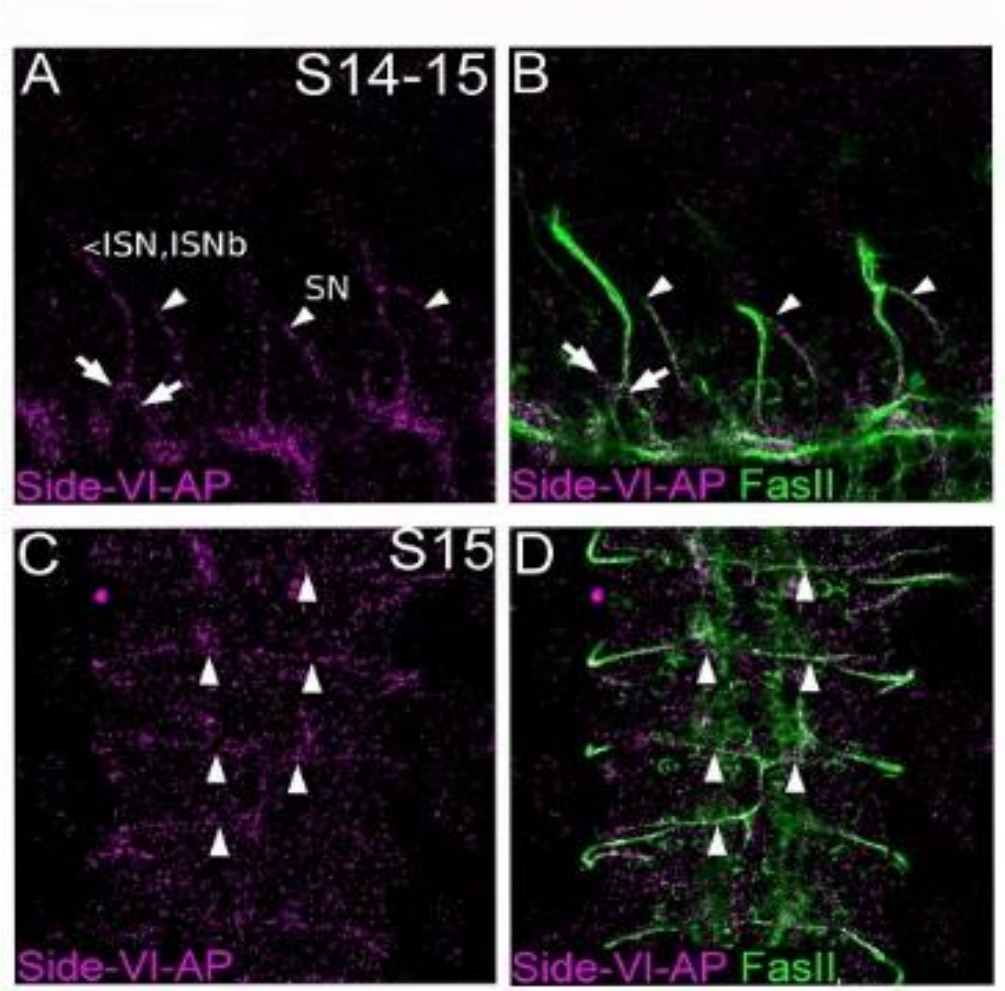

Figure 6: The Side-VI ectodomain can bind motor axons during embryonic development. Receptor Alkaline Phosphatase in situ (RAP in situ) of Side-VI-AP in a stage 14-15 wild type embryo. (A, B)

The intersegmental (ISN) and segmental (SN) motor nerves are labeled. The anterior (left) and posterior (right) tributaries of the ISN are labeled with arrows, while the SN is labeled with arrowheads in each segment. (C, D) Side-VI-AP binding to the transverse nerve (TN) above the CNS in a stage 15 embryo. The location of the TN is indicated with arrowheads. RAP in situ (magenta) is overlaid with ID4, anti-FasII staining (green) to show motor nerves in B and D.

Additionally, we also utilized the Side-VI-AP probe to stain a UAS-Beat-Vb line driven by Tub-Gal4, where we observed strong staining in the muscles of the embryos (Fig. 7).

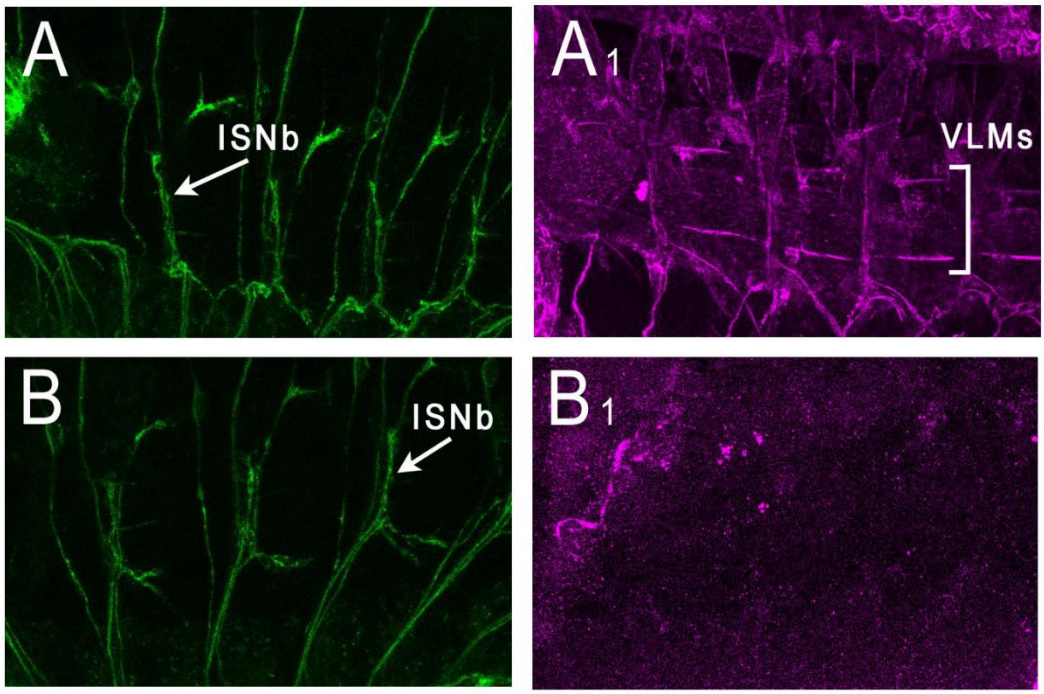

Figure 7: Side-VI binds to Beat-Vb in vivo. (A and A_1) Side-VI-AP staining of Tub-GAL4 driving UAS-Beat-V (magenta) and 1D4 (green). (B and B_1) Side-VI-AP and 1D4 staining of wild-type embryo.

Finally, to determine the specificity of the interaction between Side-VI and the Beat-V subfamily, and to assess the extent to which Beat-V paralogs had evolved differing affinities to Side-VI, we quantified their interaction biophysically through surface plasmon resonance

(SPR). We ran monomeric ectodomains from Beat-V proteins over the surface of Biacore chips layered with Side-VI to determine their binding affinities and the kinetics of the interactions. Binding data show that association and dissociation kinetics are fast, too fast to measure ($k$off $\geq 0.5\ s^{-1}$). Therefore, SPR responses are only fitted at equilibrium to a binding isotherm and their fit is indicative of specific interaction (Fig. 8A-C).

Binding for the three Beat-Vs to Side-VI is around the µM mark (0.76µM, 2.3µM and 9.4µM for Beat-Va, Beat-Vb and Beat-Vc respectively). These dissociation constants are in the same range as the ones we have previously described for interactions between Beat-Ia and Side [10] and are typical for interactions of cell adhesion molecules [28]. Our findings indicate that Side-VI constitutes a novel binding partner in vivo for the Beat-V subgroup of receptors during motor axon guidance. We find that while all Beat-V receptors interact with Side-VI, these interactions are highly specific and confirm our Bio-Plex assay. Furthermore, our results indicate that while tandem duplication has allowed a regulatory diversification of the Beat-V cluster, they have all retained the *same Side-VI ligand specificity*.

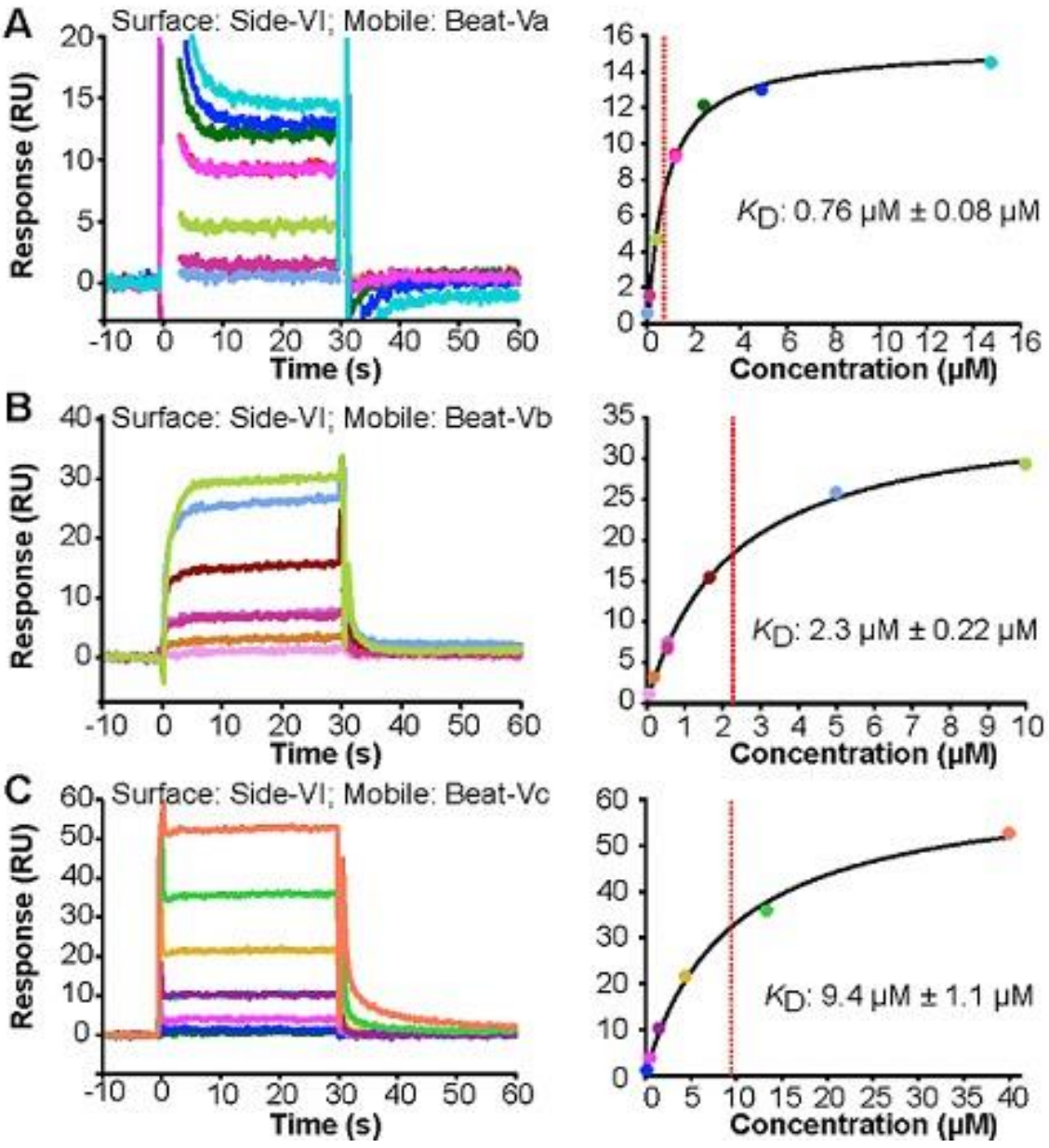

Figure 8. Surface Plasmon Resonance sensorgrams (left panels) and binding isotherms (right panels) for three Beat–Side complexes. (A-C) The interactions of Side-VI with the Beat-V family of receptors. Side-VI was captured on a Biacore SA chip, and titration series of Beat-Va (A), Beat-Vb (B), and Beat-Vc (C) were flowed over the SA chip. The ± errors represent standard error from the fitting of one titration series.

Discussion

Given their structural similarity and in vitro interaction profiles it has been proposed that the family of related Side proteins function as ligands in vivo for the Beat family of

receptors. Our phylogenetic study and the interaction profiles between Sides and Beats (Fig. 1) suggest a functional specialization of specific Sides in part to interact with individual Beat clusters such as Side-VI with the Beat-V cluster or Side-IV with the Beat-II cluster. Our results also support the hypothesis that Beats have diverged at two different levels: functional divergence of phylogenetic Beat groups at least partially to interact with different Side proteins and regulatory divergence among members within the same phylogenetic Beat cluster. Our mRNA expression analysis reveals specialization of expression within the

Beat-I and Beat-V subgroups where different members clearly favor expression in different subgroups of motor neurons (Fig. 4). While specific interaction of Side with Beat-Ia and their function in the neuromuscular system was already known [2, 4, 6, 12], our results provide several lines of evidence to support a role for Side-VI in motor axon guidance as partner for the Beat-V receptors. First, the expression patterns of Side-VI at intermediate targets of ISN and ISNb motor axons complement the expression of the Beat-V receptors in those motor nerves. Second, the overlap in the phenotypes in the ISN and ISNb of *side-VI* and *beat-Vs* mutants. Third, the specificity with which Side-VI ectodomains bind to the ISN and ISNb motor nerves where Beat-VIs are expressed. Fourth, Side-VI interacts with high specificity and affinity with the Beat-V subfamily of receptors in vivo and in vitro. Given the evolutionary distances between the Beat-I and V cluster and between Side and Side-VI (Fig. 1) our analyses strongly support that the Side family of membrane proteins indeed represents a family of interacting partners for the Beat receptors in vivo.

Promiscuity of Side-Beat interactions is preferentially restricted to one particular Side protein interacting with a particular cluster of Beat proteins, suggesting that retention of *beat-I* and *beat-V* genes following duplication could have been useful in expanding the diversity and complexity of the neuromuscular circuitry at least in two ways. Their distinct expression within the CNS could allow diverse sets of neurons to respond differently to common

Side signals, as the different Robo receptors expressed in different cells respond to its common Slit ligand [29-31]. The overlapping expression of different Beat clusters would also allow for specific combinations of receptors expressed in individual neurons to respond to different cues, as has been shown to be required in the *Drosophila* neuromuscular system [24]. Duplication could have allowed further fine tuning of affinity of interaction between individual clustered Beat paralogs and their shared Side ligands, allowing enhancement of the specificity of the response to instructive Side molecules in different neurons.

In conclusion, our results indicate that the Side family of proteins work in vivo as ligands for the Beat receptors and support a model in which the increasing developmental complexity of the insect nervous system has been mediated, in part, by the expansion of the Beat receptor family to given Side chemotropic cues.

Materials and Methods

Bioinformatics and phylogenetics

Orthologs for the *beat* and *side* genes in the 12 sequenced *Drosophila* species were established using a reciprocal BLAST approach, first against the annotated predicted transcript databases [32]. Where a full length orthologous coding sequence had not been predicted in the public databases, coding sequences of the N terminal ectodomains were inferred and annotated, aligning the full length orthologs from the closest related species against the genome assembly, and other available predicted transcripts in the host. Protein domains were inferred using the online implementations of SMART [13], HMMER [14], and DOUT-finder [15]. Multiple sequence alignments were carried out using the Muscle, t-coffee [33], and clustal-Ω [34] algorithms. Alignments were manually edited in SeaView [35] and UGENE [36]; poorly aligning sequences were removed. Maximum likelihood protein phylogenies

and bootstrap analyses were performed using RaxML source code [37] and RaxML via the CIPRES Science Gateway and visualized and edited in SeaView.

Immunohistochemistry and in situ mRNA hybridization

RAP in situ on live dissected fly embryos was carried out essentially as described in [25], using Amicon concentrated prey-AP conditioned media and binding was detected using rabbit polyclonal anti-PLAP (ABD Serotec). In situ mRNA hybridization was performed as previously described [38]. Probes were generated from cDNA vectors (Drosophila Genomics Resource Centre and *beat-Ia* cDNA kindly provided by H. Aberle) for the genes of interest and specific motor neurons were labeled in the following stocks: *RN2-Gal4::UAS-tau-myc-GFP*, *RN2-LACZ*, (23) *Lim3A-tau-myc* (22).

Chromosomal deficiencies removing *beat-V* subgroup, *Df(3R)Exel7318* was balanced over GFP chromosomes to distinguish homozygous and heterozygous embryos. Chromosomal deficiencies removing *side-VI* were crossed with *side-VI*^{MiMIC38121}. Embryos were collected and then fixed with 5% PFA, re-hydrated with decreasing concentrations of methanol and blocked with PBST containing 0.2% BSA. Mouse monoclonal primary antibodies 1D4, anti-GFP (Roche), and HRP-conjugated secondary (Jackson Immunoresearch) were used to stain embryos. After staining, embryos were incubated in DAB, hydrogen peroxide, and nickel chloride to visualize the staining patterns. Imaging was carried out on a Zeiss AxioPlan compound microscope, using a 63X oil immersion objective.

Molecular biology and cell surface binding assays

AP-fusion constructs were generated by Gateway® recombination into a destination vector, pUAS-LPGWAP, containing a metallothionein promoter N-terminal leader peptide, and C-terminal placental alkaline phosphatase. Secreted AP-ectodomains were produced in *Drosophila* S2 cells by co-transfecting the pUAS-prey-AP and pAct-Gal4 plasmids using FuGENE HD transfection reagent (Promega). Cell surface binding assays were adapted from

those previously described [39]. Briefly, 10^6 *Drosophila* S2 cells were seeded in 6-well plates, transfected with cell surface bait or control constructs, expression was induced and cells were harvested by centrifugation. Cells were washed and incubated with 0.5nM Prey-AP or LP-AP (control) conditioned S2 media for 90 minutes at room temperature and washed, and bound AP activity was measured.

Surface plasmon resonance

All Beat and Side extracellular domains with C-terminal hexahistidine tags were expressed in and secreted from *Trichoplusia ni* High Five Cells using baculoviruses. Proteins were first purified with Ni^{2+}-NTA Agarose resin, followed by size exclusion chromatography using Superdex 75 or 200 10/300 columns (GE Healthcare). For capturing on Surface Plasmon Resonance chips, the Side-VI expression construct also included a biotin acceptor peptide sequence, which was used to biotinylate using *E. coli* BirA biotin ligase, and allowed proteins to be captured on SA (streptavidin) Biacore chips (GE Healthcare). Beat-Va, -Vb, and -Vc were titrated in the mobile phase over the SA chips.

Side-VI, Beat-Va, Vb, and Vc expression constructs included complete ectodomains. Surface Plasmon Resonance experiments for Side-VI against Beat-Va, -Vb and -Vc were performed on a Biacore T100 (GE Healthcare). Unless noted, all SPR binding measurements are done in HBSp+ (GE Healthcare), which includes 10 mM HEPES pH 7.2, 150 mM NaCl, and 0.05% surfactant Polysorbate 20. To prevent non-specific binding to Biacore chip surfaces, Beat-Va and Vb binding experiments were performed with HBSp+ containing 500 mM NaCl and 15% glycerol.

Visualization of Side-VI and Beat-Va expression patterns in *Drosophila* larvae

Third instar larvae of Side-VI and Beat-Va GAL4 lines driving GFP were dissected following procedures described in Menon et al [51]. Dissected larvae were stained with rabbit

anti-GFP (Invitrogen), followed by rhodamine-conjugated anti-HRP (Jackson ImmunoResearch) and Alexa-Fluor 488 anti-rabbit (Invitrogen). Samples were imaged with a Zeiss LSM 710 with a 40X objective. Images were processed with ImageJ and Adobe Photoshop.

Side-VI--Beat-Vb in vivo interaction in *Drosophila* embryos

UAS-Beat-Vb driven by Tub-GAL4 embryos were collected and dissected following procedures described in Lee et al [52]. Dissected embryos were stained with Side-VI-AP (in S2 media), followed by primary antibodies rabbit anti-AP (Serotec) and mAb 1-D4. Secondary antibodies used were Alexa-Flour 568 anti-rabbit and Alex-Fluor 488 anti-mouse (Invitrogen). Images were collected on a Zeiss LSM 710 using a 40X objective.

References

1. Tessier-Lavigne M & Goodman C (1996) The Molecular Biology of Axon Guidance. *Science* 274(5290):1123-1133.

2. Fambrough D & Goodman CS (1996) The Drosophila beaten path gene encodes a novel secreted protein that regulates defasciculation at motor axon choice points. *Cell* 87(6):1049-1058.

3. Pipes GC, Lin Q, Riley SE, & Goodman CS (2001) The Beat generation: a multigene family encoding IgSF proteins related to the Beat axon guidance molecule in Drosophila. *Development* 128(22):4545-4552.

4. Sink H, Rehm EJ, Richstone L, Bulls YM, & Goodman CS (2001) sidestep encodes a target-derived attractant essential for motor axon guidance in Drosophila. *Cell* 105(1):57-67.

5. de Jong S, Cavallo JA, Rios CD, Dworak HA, & Sink H (2005) Target recognition and synaptogenesis by motor axons: responses to the sidestep protein. *International journal of developmental neuroscience: the official journal of the International Society for Developmental Neuroscience* 23(4):397-410.

6. Siebert M, Banovic D, Goellner B, & Aberle H (2009) Drosophila motor axons recognize and follow a Sidestep-labeled substrate pathway to reach their target fields. *Genes & development* 23(9):1052-1062.

7. Aberle H (2009) Searching for guidance cues: Follow the Sidestep trail. *Fly* 3(4).

8. Vogel C, Teichmann SA, & Chothia C (2003) The immunoglobulin superfamily in Drosophila melanogaster and Caenorhabditis elegans and the evolution of complexity. *Development (Cambridge, England)* 130(25):6317-6328.

9. Zinn K (2009) Choosing the road less traveled by: a ligand-receptor system that controls target recognition by Drosophila motor axons. *Genes & Development* 23(9):1042-1045.

10. Özkan E, *et al.* (2013) An extracellular interactome of immunoglobulin and LRR

proteins reveals receptor-ligand networks. *Cell* 154(1):228-239.

11. Ohno S (1970) *Evolution by gene duplication.* (Allen & UnwinSpringer-Verlag, London,New York) p 160.

12. Vactor DV, Sink H, Fambrough D, Tsoo R, & Goodman CS (1993) Genes that control neuromuscular specificity in Drosophila. *Cell* 73(6):1137-1153.

13. Schultz J, Milpetz F, Bork P, & Ponting CP (1998) SMART, a simple modular architecture research tool: identification of signaling domains. *Proceedings of the National Academy of Sciences of the United States of America* 95(11):5857-5864.

14. Eddy SR (2011) Accelerated Profile HMM Searches. *PLoS Computational Biology* 7(10):e1002195.

15. Novatchkova M, Schneider G, Fritz R, Eisenhaber F, & Schleiffer A (2006) DOUTfinder-identification of distant domain outliers using subsignificant sequence similarity. *Nucleic acids research* 34(Web Server issue):W214-218.

16. Lynch M & Conery JS (2000) The evolutionary fate and consequences of duplicate genes. *Science* 290(5494):1151-1155.

17. Younossi-Hartenstein A & Hartenstein V (1993) The role of the tracheae and musculature during pathfinding of Drosophila embryonic sensory axons. *Developmental biology* 158(2):430-447.

18. Harris KL & Whitington PM (2001) Pathfinding by sensory axons in Drosophila: substrates and choice points in early lch5 axon outgrowth. *Journal of neurobiology* 48(4):243-255.

19. Bate M, Rushton E, & Currie DA (1991) Cells with persistent twist expression are the embryonic precursors of adult muscles in Drosophila. *Development (Cambridge, England)* 113(1):79-89.

20. Chiang C, Patel NH, Young KE, & Beachy PA (1994) The novel homeodomain

gene buttonless specifies differentiation and axonal guidance functions of Drosophila dorsal median cells. *Development (Cambridge, England)* 120(12):3581-3593.

21. Gorczyca MG, Phillis RW, & Budnik V (1994) The role of tinman, a mesodermal cell fate gene, in axon pathfinding during the development of the transverse nerve in Drosophila. *Development (Cambridge, England)* 120(8):2143-2152.

22. Thor S, Andersson SG, Tomlinson A, & Thomas JB (1999) A LIM-homeodomain combinatorial code for motor---neuron pathway selection. *Nature* 397(6714):76-80.

23. Fujioka M, *et al.* (2003) Even-skipped, acting as a repressor, regulates axonal projections in Drosophila. *Development (Cambridge, England)* 130(22):5385-5400.

24. Zarin AA, *et al.* (2014) A Transcription Factor Network Coordinates Attraction, Repulsion, and Adhesion Combinatorially to Control Motor Axon Pathway Selection. *Neuron* 81(6):1297-1311.

25. Fox AN & Zinn K (2005) The heparan sulfate proteoglycan syndecan is an in vivo ligand for the Drosophila LAR receptor tyrosine phosphatase. *Current biology: CB* 15(19):1701-1711.

26. Wright AP, Fox AN, Johnson KG, & Zinn K (2010) Systematic screening of Drosophila deficiency mutations for embryonic phenotypes and orphan receptor ligands. *PloS one* 5(8):e12288.

27. Flanagan JG & Leder P (1990) The kit ligand: a cell surface molecule altered in steel mutant fibroblasts. *Cell* 63(1):185-194.

28. van der Merwe PA & Barclay AN (1994) Transient intercellular adhesion: the importance of weak protein-protein interactions. *Trends in biochemical sciences* 19(9):354-358.

29. Rajagopalan S, Nicolas E, Vivancos V, Berger J, & Dickson BJ (2000) Crossing the midline: roles and regulation of Robo receptors. *Neuron* 28(3):767-777.

30. Simpson JH, Kidd T, Bland KS, & Goodman CS (2000) Short-range and long-range guidance by slit and its Robo receptors. Robo and Robo2 play distinct roles in midline guidance. *Neuron* 28(3):753-766.

31. Spitzweck B, Brankatschk M, & Dickson BJ (2010) Distinct protein domains and expression patterns confer divergent axon guidance functions for Drosophila Robo receptors. *Cell* 140(3):409-420.

32. Drosophila 12 Genomes C, *et al.* (2007) Evolution of genes and genomes on the Drosophila phylogeny. *Nature* 450(7167):203-218.

33. Notredame C, Higgins DG, & Heringa J (2000) T-Coffee: A novel method for fast and accurate multiple sequence alignment. *Journal of molecular biology* 302(1):205-217.

34. Sievers F, *et al.* (2011) Fast, scalable generation of high-quality protein multiple sequence alignments using Clustal Omega. *Molecular systems biology* 7:539.

35. Gouy M, Guindon S, & Gascuel O (2010) SeaView version 4: A multiplatform graphical user interface for sequence alignment and phylogenetic tree building. *Molecular biology and evolution* 27(2):221-224.

36. Okonechnikov K, Golosova O, Fursov M, & team U (2012) Unipro UGENE: a unified bioinformatics toolkit. *Bioinformatics* 28(8):1166-1167.

37. Stamatakis A (2006) RAxML-VI-HPC: maximum likelihood-based phylogenetic analyses with thousands of taxa and mixed models. *Bioinformatics* 22(21):2688-2690.

38. Zarin AA, Daly AC, Hulsmeier J, Asadzadeh J, & Labrador JP (2012) A GATA/homeodomain transcriptional code regulates axon guidance through the Unc-5 receptor. *Development* 139(10):1798-1805.

39. Cheng HJ & Flanagan JG (1994) Identification and cloning of ELF-1, a developmentally expressed ligand for the Mek4 and Sek receptor tyrosine kinases. *Cell* 79(1):157-168.

3-Dimensional Nano-Architected Scaffolds with Tunable Stiffness for Efficient Bone Tissue Growth

Abstract

Although the precise mechanisms leading to orthopedic implant failure are not well understood, it is believed that the micromechanical environment at the bone-implant interface regulates the structural stability of an implant.

In this study, we seek to understand how the 3D mechanical environment of an implant affects bone formation during early osteointegration. To do this, we employed two-photon lithography (TPL) to fabricate 3-dimensional rigid polymer scaffolds with tetrakaidecahedral periodic geometry, herewith referred to as nanolattices, whose strut dimensions were on the same order as osteoblasts' focal adhesions (~2μm) and pore sizes of 25μm. Some of these nanolattices were subsequently coated with thin conformal layers of Ti or W, and a final outer layer of 18nm-thick TiO_2 was deposited on all samples to ensure biocompatibility. Nanomechanical experiments on each type of nanolattice revealed the range of stiffnesses to be 0.7-100MPa

Osteoblast-like cells (SAOS-2) were seeded on each nanolattice, and their mechanosensitve response was explored by tracking their mineral secretions and intracellular f-actin and vinculin concentrations after 2, 8 and 12 days of cell culture. The most compliant nanolattices exhibited ~20% more intracellular f-actin and ~40% more secreted Ca and P than the stiffer nanolattices. This work suggests that nanolattices with stiffnesses similar to that of cartilage (~0.5-3 MPa) may provide an optimal environment for bone growth. These findings help provide a greater understanding of osteoblast mechanosensitivity and have profound implications in developing more effective and safer bone prostheses.

Introduction

With the increase in the ageing population, the number of osteoporosis-related fractures is expected to grow substantially over the next twenty-five years. By 2030, the demand for hip and knee replacements is predicted to increase by 174% and 673%, respectively [1]. This tremendous need for bone prostheses has driven research and development of more effective bone implants. Autografts are bone replacements taken directly from the iliac crest of a patient and transplanted to the target site where they lead to osteointegration, osteoinduction and osteogenesis, which are necessary for a functional bone implant. While autografts virtually eliminate the risk of implant rejection, donor site morbidity and limited graft availability are significant limitations of this approach.

Significant efforts have been directed at developing fully synthetic implants for more than 5 decades [2]. Commercially available, fully synthetic orthopedic implants are primarily manufactured out of stainless steel and titanium alloys to achieve the required fatigue strength, high strength-to-weight ratio, flexibility, resistance to corrosion, and biocompatibility [3]. The stiffness of these materials is at least two orders of magnitude greater than that of cancellous bone (0.04 – 1 GPa) [4]. This discrepancy in stiffness between bone and the implant results in insufficient mechanical load transfer from the implant to the surrounding tissues, which leads to a phenomenon known as stress shielding. The bone adapts to these reduced stresses, relative to its natural state, by decreasing its mass, which prevents the bone from anchoring to the implant and leads to implant loosening and eventual failure [5-7]. Hutmacher et al. postulated that an ideal implant should retain durability in the body and have mechanical properties that match those of the natural bone that is being replaced [5]. This remains to be demonstrated experimentally, especially at the cellular level.

To date, research on mammalian cells' ability to exert forces on their substrate via stress

fibers, which are bundles of polymerized actin, has shown that cells exhibit a bell-shaped sensitivity to changes in substrate stiffness [8, 9]. We hypothesize that adhesion and mineralization behavior of bone cells may also exhibit a sensitivity dependence on the stiffness of 3-dimensional (3D) scaffolds [10-12]. The identification of an optimal stiffness range for mineralization has the potential to offer quantitative guidelines for the fabrication of bone implants that minimize stress-shielding while maximizing bone growth.

The challenges associated with fabricating complex 3-dimensional scaffolds with strut dimensions on the same order as osteoblasts (~10μm) has rendered existing studies to be limited to a stiffness window ranging from ~10-200 kPa [13-16]. As a consequence, most literature has been focused on studying cell behavior on either 2D substrates or on scaffolds with a narrow range of structural stiffness and strut size of at least one order of magnitude larger than the cell's size which has made the cell-scaffold interaction virtually the same as that on a 2D substrate [5, 13, 14, 17].

3D porous scaffolds with different pore sizes have been shown to offer an excellent platform to mimic natural physiologically relevant microenvironments [18-20]. For example, Raimondi et al. fabricated polymeric scaffolds and observed that a minimum pore size of 10μm was necessary to allow for cell infiltration into their scaffold [19]. Tayalia et al. utilized polymeric scaffolds and showed that cells are more uniformly dispersed inside scaffolds with pore sizes of 52μm compared to 12μm [20]. Harley et al. produced collagen–glycosaminoglycan scaffolds and showed that cell migration and cell speed increased by a factor of 2 when the scaffold's pore size was reduced from 151 to 96 μm [21]. Most of these studies focused on investigating the relationship between porosity and cellular behavior and none of them discusses the scaffold stiffness, which likely serves as a key factor in governing osteoblasts' mineralization abilities.

We focus on exploring the dependence of osteoblast-like cells (SAOS-2) on the structural stiffness of porous substrates with a constant pore size. We utilized two-photon lithography, sputtering and atomic layer deposition (ALD) to fabricate periodic, 3-dimensional cellular solids, referred to as nanolattices, with tetrakaidecahedral geometry, measured their structural stiffness, and populated osteoblast-like SAOS-2 cells onto them to study their behavior. The structural modulus of elasticity, or stiffness, E^*, is very sensitive to the relative density, $(\bar{r})$, of a periodic cellular solid:

$$E^* = CE_s(\bar{\rho})^m \tag{1}$$

where C is a geometry-dependent proportionality constant, E_s is the elastic modulus of the solid that comprises the solid and m is a topology-dependent power law coefficient [22]. The relative density is defined as the volume fraction of the solid material (V_s) divided by the representative volume of the unit cell (V_{uc}) [23].

$$\bar{\rho} = \frac{V_s}{V_{UC}} \tag{2}$$

$\bar{\rho}$ is a function of unit cell topology, mean pore size (U), and the ratio of beam-length to beam-radius (L/R), as shown in Fig. 1a. The relative density of the nanolattices in this work, calculated using Solidworks software (Dassault Systems), ranged from 0.14% to 12.2%. The pore size, U, was maintained constant at 25μm to isolate the effects of relative density only, which was varied by depositing different material coatings onto the original polymer nanolattices (Fig. 1). We were able to achieve a range of structural stiffnesses that spans over

two orders of magnitude, from ~0.7 MPa to 100 MPa, which covers a region that had not been previously explored: existing literature on scaffolds with similar sizes focused on a stiffness range spanning from ~10-200 kPa.

SAOS-2 cells were seeded on the nanolattices, and the cells' f-actin concentration was measured after a 48-hour growth period in mineralization media. Longer periods of growth, up to 12 days, were conducted to characterize the relationship between scaffold stiffness and cells' mineralization ability.

Materials and methods

Sample preparation

All scaffolds were fabricated via direct laser writing (DWL) two-photon lithography, which employs a femtosecond-pulsed laser that is rastered in space to selectively cross-link a negative tone photoresist, IP-Dip (Nanoscribe GmbH), into a designed structure. The resulting polymeric nanolattices were subsequently coated with different materials to create scaffolds that are comprised of 4 different material systems shown in Fig. 1a.

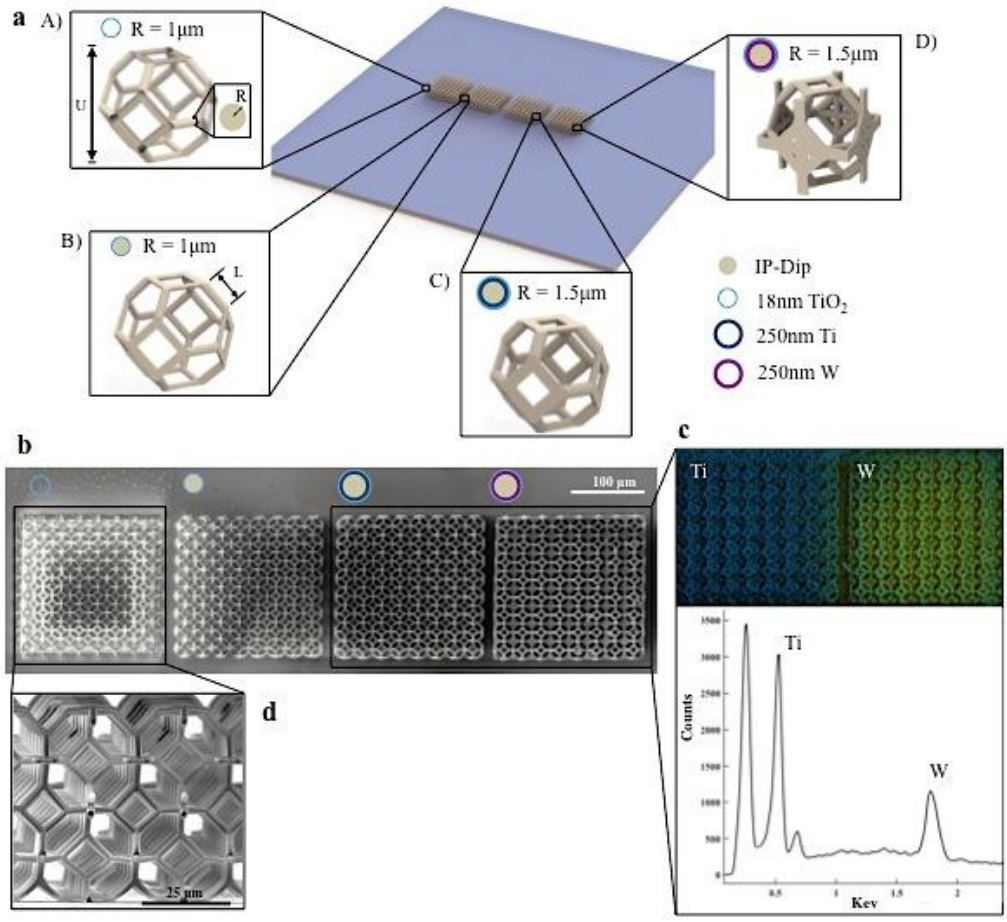

Figure 1: Design and Fabrication of the Nanolattices. (a) Computer-aided design of the sample showing the four types of nanolattices that were tested. All nanolattices had tetrakaidecahedral unit cells of length (U) = 25μm and a beam radius (R), which varied from 1 to 1.5μm. The insets show a zoomed-in view of the unit cells that comprise each type of nanolattice: (A) hollow with an 18nm-thick TiO_2 wall. (B) IP-Dip-core coated with 18nm-thick layer of TiO_2. (C) IP-Dip-core coated with ~250nm-thick layer of Ti and 18nm-thick layer of TiO_2. (D) IP-Dip-core coated with ~250nm-thick layer of W and 18nm-thick layer of TiO_2. **(b)** Top SEM view of the fabricated samples. **(c)** EDS map and spectrum that shows the composition of the W and Ti nanolattices (material systems C and D). **(d)** A zoomed-in side SEM view of the hollow TiO2 nanolattice (material system(A)).

Material system (A) was fabricated by first coating the polymer scaffold with an 18nm-thick layer of TiO_2 deposited via atomic layer deposition (ALD) and then slicing off the

sample edges along each face using a focused ion beam (FIB) (FEI Nova 200 Nanolab) at 30KeV and 5nA. The samples were then placed into an O_2 plasma etcher at 0.6 mbarr and 100W (Diener GmbH) for 24 hours to etch away the original scaffold and to produce a hollow TiO2 nanolattice (Fig. 1b, 1d).

Material system (B) was fabricated using the same process as material system (A) without etching away the polymer scaffold. **Material system (C)** was fabricated by sputtering a ~250nm-thick layer of Ti onto the original polymer scaffold and subsequently coating it with an 18nm-thick layer of TiO_2 deposited via atomic layer deposition (ALD). **Material system (D)** was fabricated by sputtering a ~250nm-thick layer of W onto the original polymer scaffold and subsequently coating it with an 18nm-thick layer of TiO_2 deposited via ALD.

Some of the original polymer nanolattices were used for fluorescence studies, which revealed the need to treat the polymer nanolattices with Sudan Black to suppress autofluorescence according to the protocol developed by Jaafar et al. [24] (supplementary information, Fig. S1).

Sputter deposition was carried out using a magnetron sputterer (Temescal BJD-1800). Titanium was sputtered using RF power at 125W, a working pressure of 6mtorr, Ar pressure of 60sccm and table rotation set at 100%. An average Ti thickness of ~250nm was obtained after depositing for 140 minutes. W was deposited using RF power of 125W, a working pressure of 5mtorr, Ar pressure of 50sccm and table rotation set at 100%. An average W thickness of ~250nm was obtained after depositing for 140 minutes. The outermost 18nm-thick TiO_2 coating was deposited using ALD (Cambridge Nanotech S200) with H_2O and Titanium Tetrachloride ($TiCl_4$) precursors. A shadow mask was used to selectively coat Ti on system (C) and W on system (D) that are adjacent to each other on the Si substrate (see supplementary material for details). Fig. 1c provides a map generated by energy dispersive spectroscopy (EDS) that shows the distribution of Ti and W in material systems (C) and (D). The spraying effect

inherent to sputtering deposition was minimized to ~15μm by reducing the size of the deposition window to 120μm x 120μm.

To mimic the porous structure of cancellous bone we chose a tessellated tetrakaidecahedral unit cell geometry (Fig. 1a) which had circular beams of length $L = 8.33\mu m$ and a radius $R = 1\mu m$ for material system (A) and (B) or $R = 1.5\mu m$ for material systems (C) and (D), and a unit cell size $U = 25\mu m$ for all material systems (Fig. 1a). Each nanolattice contained 8 (length) x 8 (width) x 2 (height) unit cells, and each sample contained 4 nanolattices arranged in a linear sequence from material system (A) to (D) to establish a stiffness gradient (Fig. 1b). The nanolattices were separated by 10μm to allow for precise and selective sputter coating (Fig. 1c).

Nanomechanical experiments

All nanolattices were uniaxially compressed to a maximum strain of 50% at a strain rate of 10^{-3} s^{-1} in a nanoindenter (G200, Agilent Technologies). The load vs. displacement data collected by the nanoindenter was converted into engineering stress vs. strain. Engineering stress was calculated using $\sigma = F/A$, where F is the applied load and A is the footprint area of the nanolattice, and global compressive strain, ε, was calculated as $\varepsilon = (H_f - H_i)/H_i$ where H_i is the initial height of the nanolattice measured from SEM images and $(H_f - H_i)$ is the displacement recordered by the nanoindenter. The structural stiffness of the nanolattice, E^*, was calculated as the slope of the elastic loading portion of the data, which is indicated by the dashed black line in Fig. 2b:

$$E^* = \frac{d\sigma}{d\varepsilon} \tag{3}$$

Cell culture

All in vitro experiments were performed using the SAOS-2 cell line from ATCC. Cells were cultured in 100 mm dishes and DMEM, supplemented with 10% fetal bovine serum (FBS), 2mM L-glutamine, 100 U ml^{-1} penicillin and 100 µg ml^{-1} streptomycin. Media was replaced every 2 days, and cells split every 4-5 days using Accutase Cell Detachment Solution. Differentiation media consisted of DMEM low glucose, with 10% FBS, 2mM L-glutamine, 100 U ml^{-1} penicillin and 100 µg ml^{-1} streptomycin, 10 mM β-glycerophosphate, 100 nM dexamethasone, and 50 µM ascorbic acid.

For immunostaining experiments, cells were seeded onto nanolattices at a density of 15,000 cells/cm^{-2} and grown for 7 days, after which they were changed into mineralization media and cultured for another 2 days. Samples were then washed three times with PBS and fixed with 4% paraformaldehyde for 15 minutes. Samples were washed again with PBS and blocked with 1% BSA in PBS for 30 minutes. Rabbit monoclonal vinculin antibody (Thermo Fisher) was diluted in blocking buffer, added to the cells, which were then incubated overnight at 4C. Samples were then washed three times with PBST incubated with Phalloidin CruzFluor™ 555 (Santa Cruz Biotechnology) and Alexa Fluor® 647 AffiniPure Donkey Anti-Rabbit (Jackson ImmunoResearch) at room temperature for three hours. Samples were washed again with PBST and imaged.

For mineralization experiments, cells were seeded onto the nanolattices at a density of 15,000 cells/cm^{-2} and allowed to proliferate for 14 days. Cells were then changed into mineralization media and cultured for another 8 or 12 days. The samples were washed three times in PBS and fixed in 4% paraformaldehyde for 15 min. After fixation, the samples were washed again with PBS, and then incubated in serial dilutions of ethanol for 10 minutes each.

Cell imaging and secretions characterization

Once the cells from subset 1 were grown on the nanolattices for 2 days in mineralization media they were imaged to quantify the amount of fluorescence coming from f-actin and vinculin staining. Samples were imaged with a Zeiss LSM 710 confocal microscope using a 20x, NA 0.8 lens, which offered the highest magnification to image the entire nanolattice. Z-stack images were captured at a constant spacing of 1μm and a total height of 55μm and were used to calculate the maximum projected intensity using software ImageJ. To quantify the relative amount of fluorescence from each material system, fluorescence data from each individual chip was normalized by the fluorescence intensity of material system (A). A total of 5 chips were used to determine error in fluorescence experiments.

To evaluate propensity for mineralization and to quantify it, SAOS-2 cells from subset 2 were subjected to serial dilutions of ethanol in phosphate buffered saline until 100% ethanol was attained and then processed in a critical point dryer (Tousimis 915B). Cell secretions were morphologically and spectroscopically analyzed using a scanning electron microscope (SEM, FEI Nova 200 Nanolab) equipped with an EDS module (EDAX Genesis 7000). EDS parameters were adopted from Maggi et al.[18], and 3 scans per nanolattice were taken to ensure current stability. Raman analysis of cell secretions deposited onto the nanolattices was carried out using a micro Raman spectrometer (Renishaw M1000) with a laser wavelength of 514.5 nm and a power density of 130W/cm^2.

Results

Nanomechanical experiments

We performed quasi-static uniaxial compression experiments to ~50% global uniaxial strain to determine the effective structural stiffness (E^*) and deformation characteristics of each nanolattice. Fig. 2 shows SEM images of nanolattices from each material system before and

after the compression, as well as the corresponding stress vs. strain data.

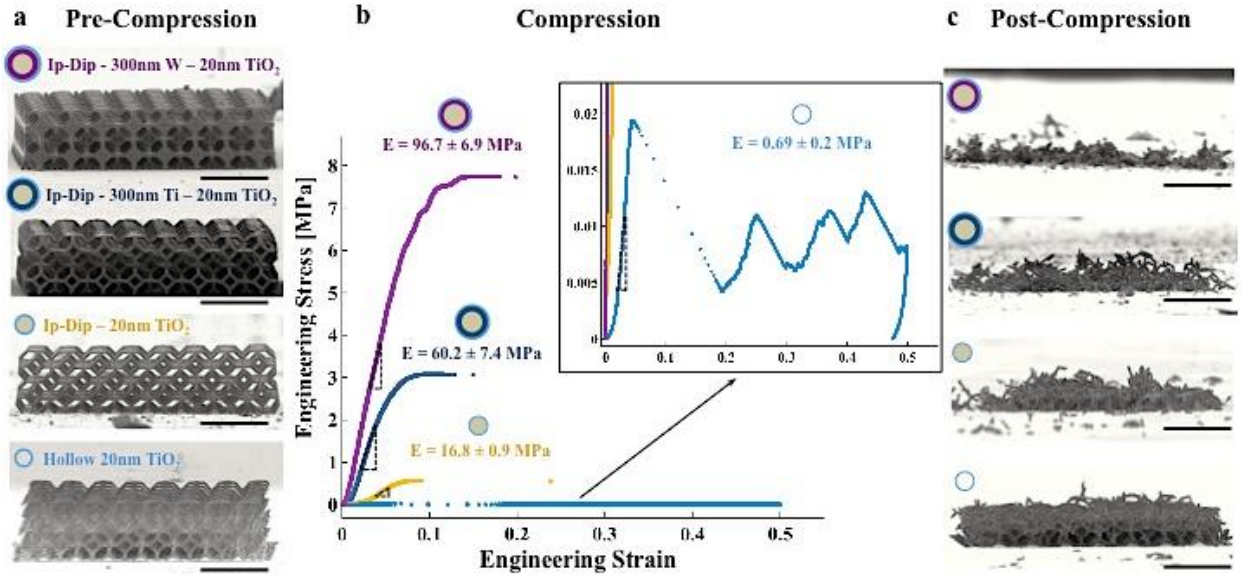

Figure 2: Uniaxial compression experiments. (a) SEM images of representative as-fabricated samples from each material system. The circles in the top left corner of each image represent a schematic of the beam cross section for each material system (not to scale). **(b)** Representative stress-strain response to quasi-static uniaxial compression of each material system. The inset shows a zoomed-in view of the compression of the hollow nanolattice (wall thickness = 18nm TiO_2). **(c)** SEM images of the same samples after compression. All samples from material systems B, C, and D underwent brittle failure, the hollow nanolattice (A) (bottom image) experienced localized Euler beam buckling and some residual recovery. Scale bars in each SEM image is 50μm.

The stress-strain data for all samples contains a short initial non-linearity, or toe region, which is primarily caused by a small misalignment between the compression tip and the top surface of the nanolattice. The stiffer material systems (C) (polymer/Ti/TiO_2) and (D) (polymer/W/TiO_2) exhibited a toe region up to 1% strain; the more compliant systems (B) (polymer/TiO_2) and (A) (hollow/TiO_2) displayed a larger toe region that extended up to 3% strain. A linear elastic region followed the toe region and is indicated by the dashed-black lines in Fig. 2b. The effective structural stiffness (E^*) was calculated using this slope [25, 26]. The post-elastic behavior varied depending on the constituent material of the nanolattice. Fig. 2c,

which shows post-compression SEM images of a representative nanolattice from each material system, reveals that all the composite systems (B, C, and D) experienced catastrophic brittle failure at a strain of ~9%, ~13% and ~18% respectively; the hollow material system (A) deformed in a ductile-like fashion with discrete serrations that correspond to individual layer buckling events (Fig. 2b-inset). Table I summarizes the moduli, E^*, and compressive strengths, σ_f, for all material systems, which span more than two orders of magnitude.

Table I: Elastic moduli (E*) and compressive strength, σ_f, of each material system measured via uniaxial quasi-static compression. Error was calculated by taking the standard deviation from 4 data points gathered per material system.

System	E* (Mpa)	σ_f (Mpa)
A	0.69 ± 0.2	0.019 ± 0.003
B	16.8 ± 0.9	0.45 ± 0.01
C	60.2 ± 7.4	1.78 ± 0.28
D	96.7 ± 6.9	4.53 ± 0.7

Cell experiments: f-actin & vinculin fluorescence microscopy

SAOS-2 cells were cultured on the nanolattices to determine the effect of substrate stiffness on the production of stress fibers and the focal adhesions by the cells. After 2 days of growth in mineralization media, the actin fibers (f-actin) were stained with phalloidin (red) and the focal adhesions were stained with anti-vinculin antibodies (green) to quantify their amounts via fluorescent experiments (Fig. 3).

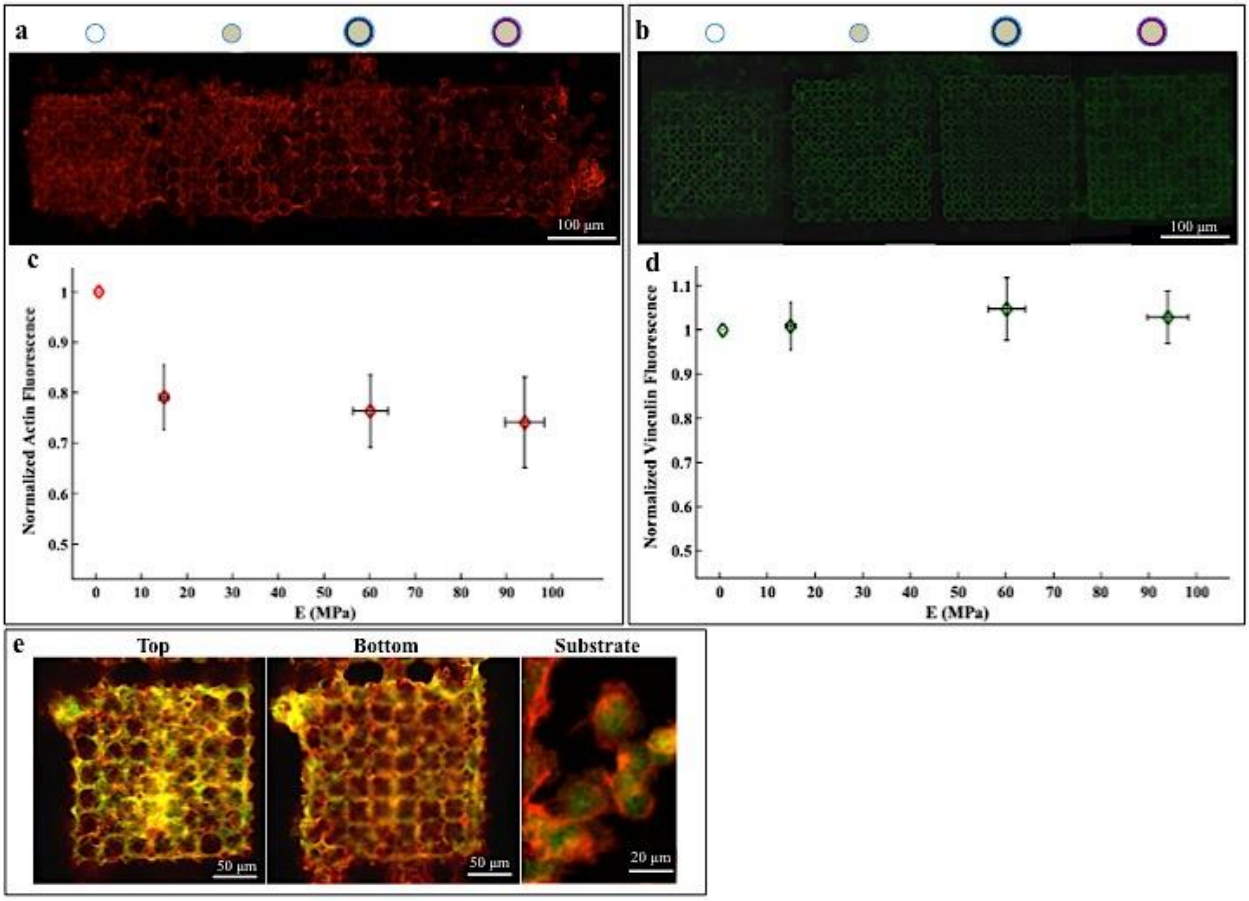

Figure 3: Fluorescence microscopy images and quantitative analysis. (a) Z-stack projections of confocal images of SAOS-2 cells grown on the nanolattices for 2 days showing actin filaments stained with phalloidin and **(b)** focal adhesions stained with anti-vinculin antibodies; the material system is represented by the schematic circle on top of the corresponding nanolattice. Relative amounts of f-actin **(c)** and focal adhesions **(d)** as a function of nanolattice stiffness. Fluorescence data was normalized by the intensity of the most compliant material system (A). Horizontal error bars represent standard deviation in nanolattice elastic moduli and vertical error bars represent standard error in fluorescence measurements. **(e)** Merging of the red and green channels shows higher levels of co-localization (yellow) on the nanolattices compared to the surrounding flat substrate.

Fig. 3a-b represents a schematic view of the material systems used in this study. The schematic representation of each individual material system is placed directly above the image that was generated via fluorescence microscopy for that specific material system (Fig. 3c-d).

Fig. 3c-d shows the results of the fluorescence experiments. Fig. 3c reveals the presence

of ~20% more f-actin on the most compliant nanolattice (A) compared to that on the other material systems (B-D), which all displayed similar levels of relative maximum intensity of f-actin. Fig. 3d shows vinculin staining which revealed no significant differences in focal adhesion concentration across the four material systems.

Merging the signal from phalloidin (Fig. 3c) and vinculin staining (Fig. 3d) produced the images in Fig. 3e, which show the amount of co-localization (yellow color) between f-actin and focal adhesions in the nanolattices. These images reveal uniform distribution of co-localized f-actin and focal adhesions along the z-axis with no apparent location preference within the nanolattice. A qualitative analysis also revealed higher levels of co-localization on the nanolattices compared to the flat substrate (Fig. 3e).

Sudan Black was not able to suppress the inherent autofluorescence of the nanolattice polymer at wavelengths shorter than ~400nm, which rendered nuclear staining, such as DAPI, ineffective in revealing meaningful information about the number of cells on each nanolattice.

The footprint area of the nanolattices occupied ~0.2% of the total sample area which made it impossible to physically separate the cells attached to the nanolattices from those on the neighboring flat substrate and to perform more quantitative biological assays.

Cell experiments: cellular secretions characterization & quantification.

Fig. 4 shows SEM images of SAOS-2 secretions on the nanolattices after a growth period of 8 and 12 days in mineralization media.

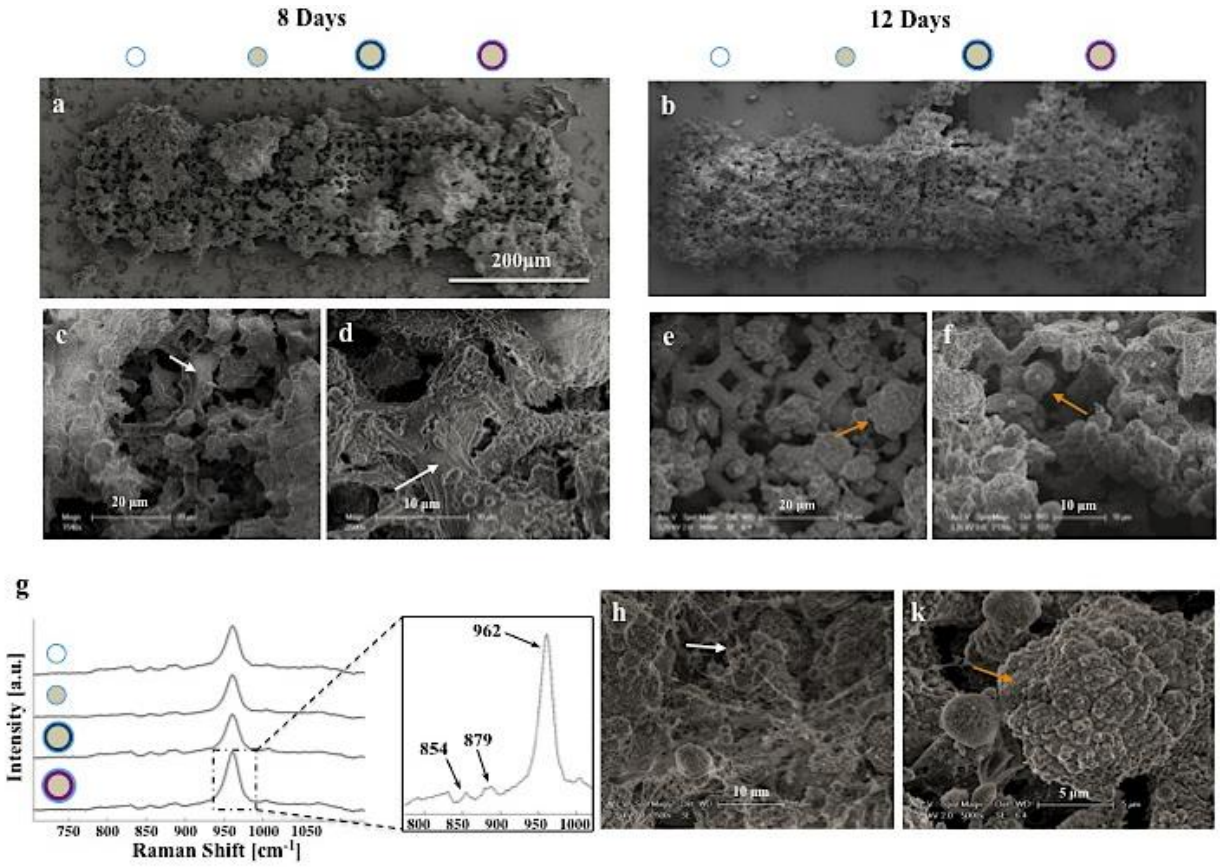

Figure 4: SEM images of the SAOS-2 cells' products after growing for 8 and 12 days in mineralization media. **(a, b) Top-down** SEM images of the samples after 8 days **(a)** and 12 days **(b)** of growth. Circles above the images in provide a schematic of the individual beam cross-section for each material system. **(c, d)** Zoomed-in SEM images revealing large amounts of organic material (white arrows) grown on the nanolattice after 8 days. **(e, f)** Zoomed-in SEM images showing large amounts of mineral formations (orange arrow) on the nanolattices after 12 days. **(g)** Raman spectroscopy analysis of SAOS-2 products after 12 days of growth. Spectra collected from all material systems revealed the presence of hydroxyapatite (962 cm^{-1}) and collagen molecules (854 cm^{-1}, 879 cm^{-1}). **(h)** SEM image of the organic phase showing the presence of filamentous features with diameters of 75 ± 32nm, consistent with the size of collagen fibrils. **(k)** SEM image of a mineral aggregate that most probably corresponds to bioapatite.

These experiments reveal that SAOS-2 cells deposited organic and mineral compounds on all nanolattices after growing in mineralization media for 8 and 12 days. SEM images in Fig. 4a-f demonstrate the presence of a continuous matrix interspersed with ~50-100nm-

diameter filaments that are indicated by arrows in Fig. 4c, d, h. Images of the mineral deposits, indicated by arrows in Fig. 4e, f, k, reveal two main morphologies: (1) spherical clusters with diameters of ~2-15μm (Fig. 4e, f) that are composed of (2) smaller aggregates ranging from ~300nm-1μm (Fig. 4k). These smaller aggregates were also present as a continuous coating on the nanolattice beams (see supplementary information for more details).

Raman spectroscopy performed on the organic phase revealed peaks at 854 cm^{-1} and 879 cm^{-1}, which most probably correspond to proline and hydroxyproline, respectively, and suggest the presence of collagen molecules. The spectra taken from the mineral phase exhibited a peak at 962cm^{-1} (Fig. 4g), which is likely representative of some form of bioapatite.

Fig. 5 shows the results of the energy dispersive spectroscopy (EDS) analysis performed on the nanolattices after 8 and 12 days of cell growth in mineralization media. All material systems revealed the presence of C, O, Na, Mg, Ca and P.

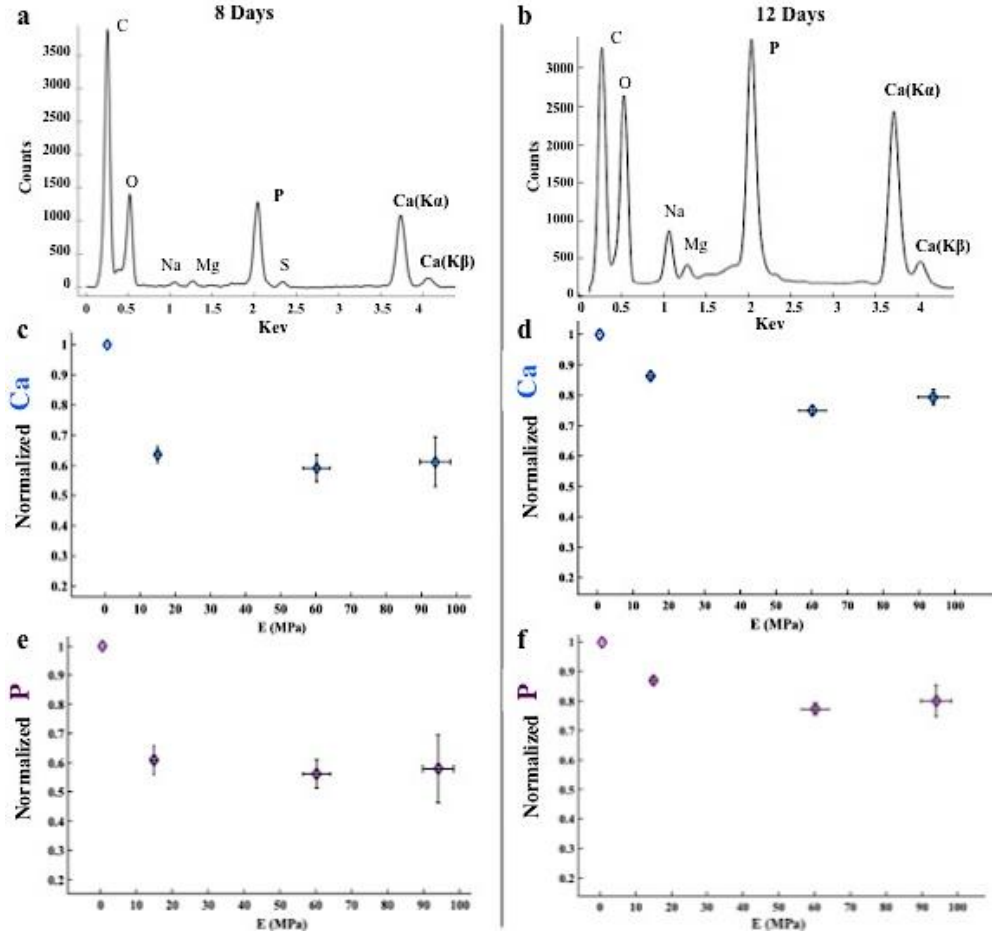

Figure 5: EDS spectra and quantification of Ca and P secreted by the SAOS-2 cells. (a, b) Representative EDS spectra after growing SAOS-2 cells for 8 days **(a)** and 12 days **(b)** in mineralization media. **(c-f)** Relative intensity of Ca (**c, d**) and P (**e, f**) after 8 days **(c, e)** and 12 days **(d, f)**. **(e, f)** Horizontal error bars represent the standard deviation in elastic moduli measured over 4 samples and vertical error bars represent the standard error in the intensity of Ca and P obtained from EDS spectra of 3 chips per time point. Ca and P concentrations were normalized by their relative amounts on the most compliant material system(A).

EDS spectra of all samples after 8 days of growth reveal the relative intensity of C to be a factor of ~3 higher than those of P and Ca; the intensity of P is ~10% higher than that of Ca (Fig. 5a). A similar EDS spectra of all samples after 12 days of growth reveal that the amount of C was ~6% lower than that of P and ~29% higher than that of Ca (Fig. 5b). Fig. 5c-f displays the relative intensity of Ca and P after 8 and 12 days of cell growth, measured via EDS, as a function of nanolattice stiffness. The data from each sample was normalized to the corresponding element intensity on the most compliant material system (A). The intrinsic inability of EDS detectors to reliably capture light elements ($z < 11$) only allowed for a qualitative analysis of C amounts on the samples that were tested.

This analysis reveals that after 8 days, the hollow, most compliant material system (A) had ~40% more Ca and P compared with those on stiffer material systems (B-D), all of which displayed similar levels of Ca and P (Fig. 5c, e). After 12 days, a less drastic difference in Ca and P concentration across the material systems was observed. Material system (A) displayed ~15% more Ca and P compared with material system (B), and material system (B) displayed ~10% more Ca and P than material systems (C) and (D) (Fig. 5d, f). These results show that material system (A), with the lowest structural modulus of 700kPa, had the highest amounts of f-actin and mineral deposits (Ca, P).

Phenomenological model

To explain the observed higher cell activity on the most compliant 3D substrates, we propose a simple phenomenological model that is aimed to relate f-actin concentration to substrate stiffness. Mammalian cells attach to a substrate by forming focal adhesions, which induce monomeric actin (g-actin) to polymerize into f-actin that can autonomously contract. F-actin pulls on the substrate by using integrins, or transmembrane proteins that serve as adhesive elements between the substrate and the cell. Rod-like protein complexes, or microtubules, resist this actin-driven cell and prevent cell collapse [27, 28].

Existing models treat actin filaments and microtubules as linear-elastic solids, which predict a linear relationship between f-actin concentration and substrate stiffness [29, 30]. This linear relationship reaches a maximum when the maximum biologically-allowed concentration of filamentous actin in the cell is reached (~60uM) [31]. These models accurately describe the interactions between f-actin and microtubules but fail to take into consideration the role of integrins, which play an important role in cell attachment and migration [32, 33].

Following the approach of De Santis et al. [34, 29] , who treated the cellular mechanical elements, f-actin and microtubules, as linear elastic springs, we developed a model that also accounts for the f-actin-integrin-substrate interaction. In this model, the cells are in static equilibrium with the substrate, and the tension generated by the filamentous actin (F_{FA}), which is a function of the force developed in the integrins (F_{IT}), is balanced by the compression of the microtubules (F_{MT}), and the traction at the cell-substrate interface (F_S) (Fig. 6a).

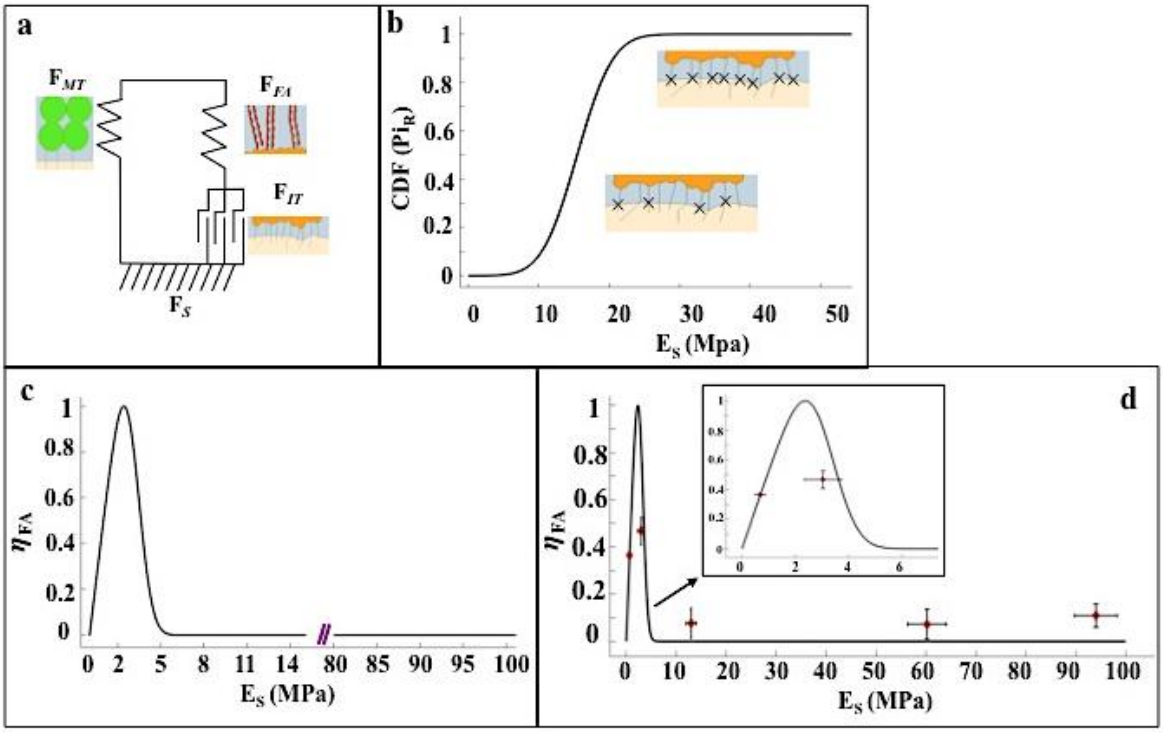

Figure 6: Substrate-dependent f-actin activation model. (a) Schematics of our mechanical model: F_{MT} represents the force exerted by microtubules (in green), F_{AF} represents the force exerted by f-actin filaments (in red) and F_{IT} represents the force exerted by integrins (in black). F_S represents the substrate resistive force. Microtubules, f-actin and the substrates were modeled as elastic solid springs while integrins were modeled as sliders.**(b)** Cumulative distribution function (CDF(Pi_R)) of a cluster of integrins per micron squared as a function of substrate elasticity showing more integrin-substrate bones breaking as stiffness increases. **(c)** Model predictions of f-actin concentration change (η_{FA}) as a function of substrate stiffness. **(d)** F-actin activation factor, η_{FA}, as a function of the structural stiffness of the substrate. Solid line represents theoretical predictions, open diamond symbols represent experimental data.

To satisfy static equilibrium, the following relation must be true:

$$F_{MT} + F_{FA} + F_S = 0 \tag{4}$$

Each force can be expressed in terms of spring constants and dimensions as:

$$F_{FA} = K_{FA}(L - L_{FAR})/L_{FAR}$$

$$F_{MT} = K_{MT}(L - L_0)/L_{FAR} \quad (5)$$

$$F_S = K_S(L - L_0)/L_0$$

where L_0 is the rest length of an element, L is the final elongation of an element, and $K = EA$ is the effective spring constant of the element where E is the Young's modulus of the element and A is the cross sectional of the element. According to this convention K_{FA} is the effective stiffness of f-actin, K_{MT} is the effective stiffness of microtubules and K_S is the effective stiffness of the substrate.

The rest lengths of the microtubule and of the substrate are independent of a cell's pre-stress, while the f-actin rest length (L_{FAR}) is a function of the pre-stress developed by a cell upon its adhesion to a substrate [34]:

$$L_{FAR} = (1 + P)L_0 \quad (6)$$

where P is a unitless pre-stress coefficient which we estimated using Engler et al. [8]. Solving equations (5) and (6) gives an expression for the force that f-actin exerts onto the substrate as a function of its stiffness:

$$F_{FA} = \frac{K_{FA}P(K_{MT} + K_S)}{K_{FA} + (K_{MT} + K_S)(1 + P)} \quad (7)$$

Eq. (8) doesn't take into account integrins, which play a crucial role in cell mechanics. Li et al. showed that a single integrin-substrate bond has a strength of ~100pN. Once the force exerted by the contracting f-actin exceeds this strength, the integrins dissociate from the substrate [35,

36]. Following the approach of Li et al. and He et al. [30, 35], we modeled the probability of an integrin-substrate bond rupture (Pi_R) as a function of actin-generated tension. We then calculated the cumulative distribution function (*CDF*) for 4000 integrins (Fig. 6b), which literature has shown to be a probable average number of integrins per μm [2, 37].

$$CDF(Pi_R) = \frac{1}{2}\int (Pi_R) dF_{FA} \tag{8}$$

We incorporated the effects of integrin-substrate bonds rupturing on the effective force exerted by f-actin by modeling integrins as sliders that work in series with the actin filaments, as shown in Fig. 6a.

Multiplying Eq. (7), which represents the linear relationship between actin force and substrate stiffness, by the probability of finding an intact integrin-substrate bond gives the f-actin activation factor, η_{FA} :

$$\eta_{FA} = \frac{\frac{K_{FA}P(K_{MT}+K_S)}{K_{FA}+(K_{MT}+K_S)(1+P)}\,(1-CDF(Pi_R))}{F_{FA(\max)}} \tag{9}$$

η_{FA} describes the change in f-actin concentration relative to the baseline level of 0, which corresponds to the minimum amount of polymerized actin necessary for the cell to remain attached to a substrate, to a maximum level of 1, which corresponds to the highest possible effective concentration of f-actin in the cell.

Eq. 9 demonstrates that η_{FA} is related to the probability of integrins dissociating from the substrate which is in turn a function of the force that f-actin exerts (Eq. 8) that is related to the substrate stiffness, K_s, as shown in Eq. 8.

η_{FA} was normalized by the maximum force that f-actin can exert, which is dictated by the maximum concentration of actin allowed by the cell.

Fig. 6c shows a plot of η_{FA} as a function of the substrate modulus ($E_s = K_s/A$) calculated by the model which reveals a linear increase in actin activation with substrate stiffness up to ~2MPa where the role of integrin dissociation becomes dominant. The maximum f-actin activation occurs at the substrate stiffness of 2.3 MPa where about 20% of the integrin-substrate bonds have broken (Fig. 6b). As more integrin-substrate bonds dissociate, η_{FA} rapidly decreases back to the baseline level of 0 at the substrate stiffness of 5.2 MPa, where virtually 100% of the integrin-substrate bonds have broken and only the baseline integrin-substrate bonds, essential for the cell-substrate attachment, remain.

The genesis of this model was motivated by Li et al., He et al. and Deshpande et al. who recognized the crucial role of integrin dynamics in cell attachment.

The model predicts a narrow range of substrate stiffnesses where the f-actin activation factor rises from 0 to 1 and then rapidly decays back to the baseline level for all higher stiffnesses.

In reality the rise and decay of η_{FA} would probably be more gradual given the dynamic nature of integrin-substrate bond kinetics. This simple model is not able to capture the kinetics of the integrin-substrate bond therefore the steady state approximation was employed.

To evaluate the credibility of the proposed model, we fabricated an additional material system, a polymer skeleton with a tetrakaidecahedral unit cell, pore size U = 25μm, beam radius of 0.5 μm coated with an 18-nm-thick TiO_2 layer, whose structural stiffness was measured to be ~3MPa, i.e. within the range of non-zeroη_{FA}. We conducted the same f-actin fluorescence experiments on these samples after growing SAOS-2 cells on them for 2 days in mineralization media (see supplementary information for more details).

Figure 6d shows the experimental data plotted together with the model. The f-actin fluorescence intensity represents the degree of f-actin activation. Given the semi-quantitative nature of fluorescence microscopy only the relative difference in fluorescence intensity between the most compliant nanolattice and all the other material systems was meaningful therefore the experimental results were plotted on the theoretical model by scaling the experimental data such that the most complaint material system agreed with the model.

It appears that the proposed phenomenological framework that is based on coupling the probability of integrins dissociating from the substrate to the existing linear elastic models for cell mechanics accurately captures the experimental observations in the range of stiffnesses studied, 0.7 to 100MPa.

Discussion

The global need for more effective osteogenic scaffolds has motivated a heated debate on the optimal scaffold specifications, especially about the mechanical properties like scaffold stiffness and strength [15, 38]. At the macroscale, it has been shown that implants with elastic moduli on the order of hundreds of GPa cause stress shielding, which hinders long-term bone healing [6]. The fundamental causes of stress shielding likely originate at the microscale and remain largely unknown. This work helps to determine and to quantify the effects of structural stiffness, i.e. modulus, of 3-dimensional nano-architected scaffolds on the stress distribution and mineralization capability of osteoblast-like cells (SAOS-2).

Mechanical characterization

A relatively large span of relative densities, 0.14%-12.2%, coupled with open cellular architecture (tetrakaidecahedron), and using different thin film coatings enabled us to fabricate 3-dimensional scaffolds that spanned more than two orders of magnitude in structural stiffness,

~0.7-100 MPa. The mechanical behavior of the nanolattices was analyzed via quasi-static uniaxial compression experiments, which revealed two distinct deformation behaviors: global brittle failure exhibited by composite material systems (B), (C) and (D), and layer-by-layer collapse exhibited by hollow material system (A). A toe region was present in all compressions up to ~3% strain and was caused by: (1) a slight initial misalignment between the 600μm–diameter compression tip and the 200μm–wide nanolattice, and (2) the incomplete initial contact caused by the concavity of the top nanolattice surface which developed during fabrication (see supplementary material, Fig. S5, for more details.) Following the toe region, nanolattices made from material system (A) (hollow TiO_2 nanolattice with 18nm wall thickness) underwent linear elastic loading up to 5% strain and a stress of 12 kPa, followed by a series of strain bursts that correspond to individual beam buckling events, which ultimately led to brittle fracture of the TiO_2 beam wall [26]. The initial strain burst was always the most extensive, ~10%, subsequent strain bursts were ~5%. This discrepancy between the initial and latter bursts is most likely a result of the substantial accumulation of strain energy in the fully intact sample during loading until the first instability/buckling event, after which the nanolattice becomes somewhat damaged and is not able to sustain as much strain energy.

Material system (B) (polymer -18nm thick TiO_2) displayed initial linear-elastic behavior up to 3% strain and ~0.3MPa stress. Inelastic deformation commenced at stresses higher than ~0.3 MPa, which generated high tensile, so-called "hoop", stresses in the outer TiO2 shell at the nodal connections of the nanolattice and caused brittle fracture of the entire beams and nodes and led to catastrophic collapse of the entire nanolattice [39, 40]. Material system (C) (polymer-Ti-TiO_2) and (D) (polymer-W-TiO_2), each containing 26% metal by volume, exhibited similar mechanical behavior characterized by an initial linear elastic response up to ~5% strain followed by yielding and limited plasticity of the composite beams. Global brittle failure occurred at a compressive stress of ~3 MPa for material system (C) and

at ~8 MPa for material system (D) because the latter is ~1.5 times stiffer. The ensuing structural collapse occurred because of inefficient load re-distribution within the nanolattice after fracture of the individual nodes and beams which disabled the nanolattice to be capable of carrying the applied compressive load.

Cell Response: f-actin and vinculin distribution

Physical cues, such as substrate stiffness, are known to affect cellular stress states, which activate pathways that control cell behavior [10]. Studies have shown that stem cell differentiation fate has a bell-shaped dependency on substrate stiffness. For example, stem cells grown on soft 2D substrates (0.1~1kPa) had a higher probability of developing into neurons while those grown on stiffer substrates (20~80kPa) had a higher probability to develop into bone cells [8, 9, 41]. The large stiffness range of 0.7-100 MPa exhibited by the 4 fabricated material systems in this work allowed us to determine the role of the 3D scaffold stiffness on osteoblasts with regards to stress fibers concentration, cell adhesion, and mineral deposition. Fluorescence microscopy data revealed the presence of stress fibers (f-actin) and focal adhesions in SAOS-2 cells grown in mineralization media for 2 days on all 4 material systems. By measuring relative fluorescence intensity we observed that f-actin expression peaked on the most compliant nanolattices made from material system (A) and dropped by ~20% with increasing nanolattice stiffness (Fig. 3a). This suggests that osteoblasts may be highly sensitive to substrate elasticity within a narrow substrate stiffness range of ~0.1-10MPa and virtually insensitive to it beyond this range. We postulate that when cells grow on a nanolattice with an elastic modulus larger than ~5MPa, the f-actin exerts forces that are larger than the tensile strength of the integrin-substrate bond, on the order of 100pN which causes its rupture. When this bond dissociates the stiffness felt by the contracting actin filaments rapidly decreases and leads to f-actin depolymerization, which manifests itself as a decrease in fluorescence intensity.

Fluorescence results also revealed that the spatial distribution of the actin filaments

appears to be a function of substrate stiffness. Figure 3a shows that the f-actin was uniformly distributed on the nanolattices of material system (A) and more confined to the nanolattice beams on nanolattices made from material systems (B), (C) and (D). The excessive number of cells present on all nanolattices and the limitations in optical resolution of the instrument prevented us from drawing more quantitative conclusions about the spatial distribution of f-actin on the nanolattices. Focal adhesion staining revealed no significant differences across material systems. Vinculin was observed along the nanolattice beams, which appear to provide anchor points for cell adhesion (Fig. 3b).

This result may be explained by the functional differences between f-actin and focal adhesions. F-actin serves as an active mechanical element that constantly pulls on the substrate, its function has been reported to be strongly sensitive to substrate stiffness Focal adhesions are passive mechanical elements that function as bridges for cell adhesion to the substrate regardless of its stiffness [42]. This functional difference may explain why vinculin appears to be more sensitive to the availability of free surface area than to the substrate stiffness. All nanolattices in this work had a similar surface area available for cell attachment, which could explain the similarity in focal adhesion concentrations across material systems.

Overlaying f-actin and vinculin fluorescence images allowed to qualitatively observe a high degree of co-localization across all material systems (Fig. 3c) which was previously observed when cells were grown in natural 3D environments derived from living tissues [43, 44]. This finding suggests that the nanolattices used in this study provide 3D platforms that may adequately mimic natural microenvironments and elicit a cellular response comparable to that seen in vivo.

Cell Response: mineralization

After growing SAOS-2 cells on the nanolattices for 8 and 12 days in mineralization

media, we observed significant cellular activity manifested by the deposition of minerals and an organic matrix onto the nanolattices. SEM images shown in Fig. 4 reveal the presence of such deposits on all nanolattices that had two main morphologies: (1) organic cellular/proteinaceous matrix interspersed with ~50-100nm-wide filaments, which are consistent with collagen deposited by osteoblasts on 2D and 3D scaffolds [45] (Fig. 4c,d,h), and (2) irregularly-shaped ~300-900nm-sized mineral aggregates which appear to be evenly distributed among the lattice beams (Fig. 4e,f; Fig. S3). These smaller formations appear form larger, cauliflower-shaped aggregates, with dimensions of ~2-15μm. These types of deposits have been observed and identified as calcium phosphate species in our earlier work [18, 46] (Fig. 4e, f, k).

Raman spectroscopy of the smaller secretions reveals the presence of several nucleic acids, fats and amino acids specifically proline and hydroxyproline, which are indicative of collagen (supplementary information, Fig. S6). Analysis of the larger, cauliflower-shaped deposits, indicates the presence of some form of bioapatite, which is the main mineral found in mature bone (Fig. 4g). These findings suggest that full osteogenic functionality was induced on the nanolattices.

Energy dispersive spectroscopy (EDS) conveyed that the SAOS-2 cells that resided on the most compliant nanolattice (material system (A)) exhibited ~40% higher levels of Ca and P compared with those on all other samples after growing in mineralization media for 8 days and ~10% higher after a growth period of 12 days. The relative amounts of Ca and P across material systems (B-D) after 8 and 12 days of cell growth remained relatively constant.

After a cell growth period of 12 days the difference in Ca and P between material system (A) and the other material systems (B-D) was much smaller (~10%) than that observed after 8 days (~40%).

These results suggest that: (1) mineral secretions occur more readily on the most compliant substrate and (2) that after a certain number of days the growth saturates. The large reduction in the mineral amounts difference between the most compliant system (A) and the other material systems also implies that rate of secretion is non-linear.

SEM images and EDS data also convey that the relative amounts of organic matrix quantified as the relative intensity of the C signal with respect to Ca and P decreased with time. C intensity went from being ~3 times greater than that of Ca and P on day 8 to approximately the same for all three elements on day 12 across all material systems.

These results are consistent with existing in-vivo models that osteoblasts initially secrete an organic extracellular matrix, mainly composed of collagen, and over time this predominantly organic matrix gets mineralized by osteoblasts with several calcium-phosphate compounds [47, 48]. This finding further suggests that the nanolattices presented in this work may be able to evoke a cellular response similar to that observed in in-vivo studies, which render them a promising framework for future implants.

Elastic moduli on the order of 0.45 to 1MPa are typical of articular cartilage, which is the natural precursor of bone in mammals [49]. The results of this work suggest that utilizing 3D scaffolds with elastic moduli in that range may be promising in stimulating more efficient bone formation by mimicking embryonic development.

Concluding remarks

We employed two-photon lithography (TPL) to fabricate 3-dimensional rigid polymer nanolattices, whose strut dimensions were on the same order as osteoblasts' focal adhesions (~2μm) and pore sizes of 25μm. Some of these nanolattices were subsequently coated with thin conformal layers of Ti or W, and a final outer layer of 18nm-thick TiO_2 was deposited on all samples to ensure biocompatibility. Nanomechanical experiments on each type of nanolattice revealed the range of stiffnesses to be ~0.7-100MPa. Osteoblast-like SAOS-2 cells were seeded

on each type of nanolattice, and their mechanosensitive response was explored by tracking the intracellular f-actin and vinculin concentration after 2 days of cell culture. Osteogenic functionality of the cells was quantified by measuring the deposited amounts of minerals after 8 and 12 days of cell growth.

These experiments revealed that the most compliant nanolattices, with the stiffness of 0.7 MPa, had a ~20% higher concentration of intracellular f-actin and ~40% more secreted Ca and P compared with all other nanolattices, where such cellular response was virtually indistinguishable.

We developed a simple phenomenological model that appears to capture the experiment observations. The underlying physical foundation of this model comes from incorporating the crucial role that integrins have in cell adhesion into well-established cell mechanics models.

The combination of the experiments and proposed theory suggest that the cell mineralization-inducing ability of 3D substrates is very sensitive to their structural stiffness and that optimal osteoblast functionality is attained on 3D substrates whose stiffness ranges from 0.7 to 3 MPa, similar to that of cartilage. These findings have significant implications for understanding the role of that 3D scaffold stiffness plays in inducing mineralization and for introducing the nanolattices as promising platforms for new synthetic bone graft materials.

References

1. Garellick, G. *et al.* Arthroplasty Future Clinical and Economic Impact of Revision Total Hip and Knee Future Clinical and Economic Impact of Revision Total Hip and Knee Arthroplasty. *J Bone Jt. Surg Am* **89,** 144–151 (2007).

2. Roberts, T. T. & Rosenbaum, A. J. Bone grafts, bone substitutes and orthobiologics: the bridge between basic science and clinical advancements in fracture healing. *Organogenesis* **8,** 114–24 (2012).

3. Kilpadi, K. L., Chang, P. L. & Bellis, S. L. Hydroxylapatite binds more serum proteins, purified integrins, and osteoblast precursor cells than titanium or steel. *J. Biomed. Mater. Res.* **57,** 258–267 (2001).

4. Niinomi, M. & Nakai, M. Titanium-based biomaterials for preventing stress shielding between implant devices and bone. *Int. J. Biomater.* **2011,** (2011).

5. Hutmacher, D. W. Scaffolds in tissue engineering bone and cartilage. *Biomaterials* **21,** 2529–2543 (2000).

6. Huiskes, R. Stress shielding and bone resorption in THA: clinical versus computer-simulation studies. *Acta Orthop. Belg.* **59 Suppl 1,** 118–129 (1993).

7. Nagels, J., Stokdijk, M. & Rozing, P. M. Stress shielding and bone resorption in shoulder arthroplasty. *J. Shoulder Elb. Surg.* **12,** 35–39 (2003).

8. Engler, A. J., Sen, S., Sweeney, H. L. & Discher, D. E. Matrix Elasticity Directs Stem Cell Lineage Specification. *Cell* **126,** 677–689 (2006).

9. Murphy, W. L., McDevitt, T. C. & Engler, A. J. Materials as stem cell regulators. *Nat. Mater.* **13,** 547–557 (2014).

10. Discher, D. E., Janmey, P. & Wang, Y.-L. Tissue cells feel and respond to the stiffness of their substrate. *Science* **310,** 1139–43 (2005).

11. Pedersen, J. A. & Swartz, M. A. Mechanobiology in the third dimension. *Ann. Biomed.*

Eng. **33,** 1469–1490 (2005).

12. Wu, S., Liu, X., Yeung, K. W. K., Liu, C. & Yang, X. Biomimetic porous scaffolds for bone tissue engineering. *Mater. Sci. Eng. R Reports* **80,** 1–36 (2014).

13. Cui, Y. *et al.* The nanocomposite scaffold of poly(lactide-co-glycolide) and hydroxyapatite surface-grafted with l-lactic acid oligomer for bone repair. *Acta Biomater.* **5,** 2680–2692 (2009).

14. Fu, Q., Saiz, E., Rahaman, M. N. & Tomsia, A. P. Bioactive glass scaffolds for bone tissue engineering: State of the art and future perspectives. *Mater. Sci. Eng. C* **31,** 1245–1256 (2011).

15. Wagoner Johnson, A. J. & Herschler, B. A. A review of the mechanical behavior of CaP and CaP/polymer composites for applications in bone replacement and repair. *Acta Biomater.* **7,** 16–30 (2011).

16. Karageorgiou, V. & Kaplan, D. Porosity of 3D biomaterial scaffolds and osteogenesis. *Biomaterials* **26,** 5474–5491 (2005).

17. Fu, Q., Saiz, E. & Tomsia, A. P. Bioinspired strong and highly porous glass scaffolds. *Adv. Funct. Mater.* **21,** 1058–1063 (2011).

18. Maggi, A., Allen, J., Desai, T. & Greer, J. R. Osteogenic cell functionality on 3-dimensional nano-scaffolds with varying stiffness. *Extrem. Mech. Lett.* **13,** 1–9 (2017).

19. Raimondi, M. T. *et al.* Three-dimensional structural niches engineered via two-photon laser polymerization promote stem cell homing. *Acta Biomater.* **9,** 4579–4584 (2013).

20. Tayalia, P., Mendonca, C. R., Baldacchini, T., Mooney, D. J. & Mazur, E. 3D cell-migration studies using two-photon engineered polymer scaffolds. *Adv. Mater.* **20,** 4494–4498 (2008).

21. Harley, B. A. C. *et al.* Microarchitecture of three-dimensional scaffolds influences cell migration behavior via junction interactions. *Biophys. J.* **95,** 4013–4024 (2008).

22. Ashby, M. F. The properties of foams and lattices. *Philos. Trans. A. Math. Phys. Eng. Sci.* **364,** 15–30 (2006).

23. Gibson, L. J. & Ashby, M. F. *Cellular solids: Structure and properties*. *Materials Science and Engineering: A* **123,** (1990).

24. Jaafar, I. H. *et al.* Improving fluorescence imaging of biological cells on biomedical polymers. *Acta Biomater.* **7,** 1588–1598 (2011).

25. Montemayor, L. C. & Greer, J. R. Mechanical Response of Hollow Metallic Nanolattices: Combining Structural and Material Size Effects. *J. Appl. Mech.* **82,** 1–10 (2015).

26. Meza, L. R. & Greer, J. R. Mechanical characterization of hollow ceramic nanolattices. *J. Mater. Sci.* **49,** 2496–2508 (2014).

27. Wang, N., Butler, J. P. P. & Ingber, D. E. E. Mechanotransduction across the cell surface and through the cytoskeleton. *Science* **260,** 1124–1127 (1993).

28. Rodriguez, M. L., McGarry, P. J. & Sniadecki, N. J. Review on cell mechanics: Experimental and modeling approaches. *Appl. Mech. Rev*. **65,** 060801 (2013).

29. McGarry, J. G. & Prendergast, P. J. A three-dimensional finite element model of an adherent eukaryotic cell. *Eur. Cell. Mater.* **7,** 27–33; discussion 33–34 (2004).

30. He, S., Su, Y., Ji, B. & Gao, H. Some basic questions on mechanosensing in cell-substrate interaction. *J. Mech. Phys. Solids* **70,** 116–135 (2014).

31. Milo, R. & Phillips, R. *Cell Biology By the Numbers*. *Current opinion in plant biology* (2014). doi:10.1016/j.pbi.2009.10.009

32. Elosegui-Artola, A. *et al.* Rigidity sensing and adaptation through regulation of integrin types. *Nat. Mater.* **13,** 631–7 (2014).

33. Cavalcanti-Adam, E. A. *et al.* Cell spreading and focal adhesion dynamics are regulated by spacing of integrin ligands. *Biophys. J.* **92,** 2964–74 (2007).

34. De Santis, G. *et al.* How can cells sense the elasticity of a substrate? an analysis using

a cell tensegrity model. *Eur. Cells Mater.* **22,** 202–213 (2011).

35. Li, F., Redick, S. D., Erickson, H. P. & Moy, V. T. Force measurements of the alpha5beta1 integrin-fibronectin interaction. *Biophys. J.* **84,** 1252–1262 (2003).

36. Deshpande, V. S., Mrksich, M., McMeeking, R. M. & Evans, A. G. A bio-mechanical model for coupling cell contractility with focal adhesion formation. *J. Mech. Phys. Solids* **56,** 1484–1510 (2008).

37. Gefen, A. *Cellular and biomolecular mechanics and mechanobiology*. *Computer Methods in Biomechanics and Biomedical Engineering* (2012). doi:10.1080/10255842.2012.705081

38. Gibson, L. J. Biomechanics of cellular solids. *J. Biomech.* **38,** 377–399 (2005).

39. Bauer, J., Hengsbach, S., Tesari, I., Schwaiger, R. & Kraft, O. High-strength cellular ceramic composites with 3D microarchitecture. *Proc. Natl. Acad. Sci. U. S. A.* **111,** 2453–8 (2014).

40. Meza, L. R. *et al.* Resilient 3D hierarchical architected metamaterials. *Proc. Natl. Acad. Sci. U. S. A.* **112,** 11502–7 (2015).

41. Mousavi, S. J. & Hamdy Doweidar, M. Role of mechanical cues in cell differentiation and proliferation: A 3D numerical model. *PLoS One* **10,** 1–23 (2015).

42. Soediono, B. *Lodish- Molecular cell Biology*. *Journal of Chemical Information and Modeling* **53,** (1989).

43. Baker, B. M. & Chen, C. S. Deconstructing the third dimension - how 3D culture microenvironments alter cellular cues. *J. Cell Sci.* **125,** 3015–3024 (2012).

44. Cukierman, E. Taking Cell-Matrix Adhesions to the Third Dimension. *Science (80-.).* **294,** 1708–1712 (2001).

45. Venugopal, J. *et al.* Biomimetic hydroxyapatite-containing composite nanofibrous substrates for bone tissue engineering. *Philos. Trans. A. Math. Phys. Eng. Sci.* **368,** 2065–2081

(2010).

46. Verma, D., Katti, K. S. & Katti, D. R. Osteoblast adhesion, proliferation and growth on polyelectrolyte complex-hydroxyapatite nanocomposites. *Philos. Trans. A. Math. Phys. Eng. Sci.* **368,** 2083–97 (2010).

47. Gilbert SF. Developmental Biology. Osteogenesis: The Development of Bones. *Dev. Biol. 6th Ed.* http://www.ncbi.nlm.nih.gov/books/NBK10056/ (2000). doi:10: 0-87893-243-7

48. Owen, T. A. *et al.* Progressive development of the rat osteoblast phenotype in vitro: Reciprocal relationships in expression of genes associated with osteoblast proliferation and differentiation during formation of the bone extracellular matrix. *J. Cell. Physiol.* **143,** 420–430 (1990).

49. Mansour, J. M. Biomechanics of Cartilage. *Kinesiol. Mech. pathomechanics Hum. Mov.* 66–79 (2009). doi:10.1002/art.23548